

Fault creep along the southern San Andreas from interferometric synthetic aperture radar, permanent scatterers, and stacking

Suzanne Lyons and David Sandwell

Scripps Institution of Oceanography, La Jolla, California, USA

Received 13 February 2002; revised 23 September 2002; accepted 13 November 2002; published 28 January 2003.

[1] Interferometric synthetic aperture radar (InSAR) provides a practical means of mapping creep along major strike-slip faults. The small amplitude of the creep signal (<10 mm/yr), combined with its short wavelength, makes it difficult to extract from long time span interferograms, especially in agricultural or heavily vegetated areas. We utilize two approaches to extract the fault creep signal from 37 ERS SAR images along the southern San Andreas Fault. First, amplitude stacking is utilized to identify permanent scatterers, which are then used to weight the interferogram prior to spatial filtering. This weighting improves correlation and also provides a mask for poorly correlated areas. Second, the unwrapped phase is stacked to reduce tropospheric and other short-wavelength noise. This combined processing enables us to recover the near-field (~200 m) slip signal across the fault due to shallow creep. Displacement maps from 60 interferograms reveal a diffuse secular strain buildup, punctuated by localized interseismic creep of 4–6 mm/yr line of sight (LOS, 12–18 mm/yr horizontal). With the exception of Durmid Hill, this entire segment of the southern San Andreas experienced right-lateral triggered slip of up to 10 cm during the 3.5-year period spanning the 1992 Landers earthquake. The deformation change following the 1999 Hector Mine earthquake was much smaller (<1 cm) and broader than for the Landers event. Profiles across the fault during the interseismic phase show peak-to-trough amplitude ranging from 15 to 25 mm/yr (horizontal component) and the minimum misfit models show a range of creeping/locking depth values that fit the data.

INDEX TERMS: 1206 Geodesy and Gravity: Crustal movements—interplate (8155); 1243 Geodesy and Gravity: Space geodetic surveys; 1294 Geodesy and Gravity: Instruments and techniques; *KEYWORDS:* creep, southern San Andreas, InSAR, atmospheric effects

Citation: Lyons, S., and D. Sandwell, Fault creep along the southern San Andreas from interferometric synthetic aperture radar, permanent scatterers, and stacking, *J. Geophys. Res.*, 108(B1), 2047, doi:10.1029/2002JB001831, 2003.

1. Introduction

[2] Standard models of the earthquake cycle [e.g., *Tse and Rice*, 1986] assume that above a depth of about 30 km, plate boundary deformation occurs on discrete faults. Over a period of many earthquake cycles, the displacement is uniform with depth such that the sum of the preseismic, coseismic, postseismic, and interseismic deformation is equal to the geologic displacement. The depth and extent of surface creep is an important issue for both earthquake physics and earthquake hazards mitigation. Some faults remain locked over the entire thickness of the seismogenic zone throughout the earthquake cycle and so can store maximum seismic moment. Other faults slide freely from the surface to the base of the seismogenic zone and, therefore, may be less hazardous [*Bürgmann et al.*, 2000]. This slow movement of the Earth's surface at a fault is known as creep.

[3] Fault friction models [e.g., *Weertman*, 1964; *Savage and Burford*, 1971; *Tse and Rice*, 1986] relate slip at depth to surface displacement. Therefore, one can examine the spatial distribution of crustal displacement over a long period of

time (>5 years) to detect the interseismic signal and determine if a fault is creeping during that time. Creep can be gradual (months to years) or it can occur in short episodes known as “creep events” (lasting hours to days). While creep meters have excellent temporal sampling, they lack the spatial coverage needed to determine the depth variations in aseismic slip. Networks of other geodetic measurements, such as continuous GPS receivers or survey-mode GPS sites, can provide adequate temporal coverage of the coseismic, postseismic, and interseismic motions along the North American-Pacific plate boundary, but the network must be sufficiently dense for accurate determination of the average slip distribution with depth [*Thatcher*, 1983; *Harris and Segall*, 1987; *Lorenzetti and Tullis*, 1989; *Savage*, 1990; *Savage and Lisowski*, 1993]. Interferometric synthetic aperture radar (InSAR) complements these systems by providing complete 200-m spatial resolution, but at a much lower sampling rate (>35 days) than other instruments.

2. Southern San Andreas Fault and Synthetic Aperture Radar

[4] The San Andreas Fault has shown evidence for both steady creep and triggered creep over the last few decades

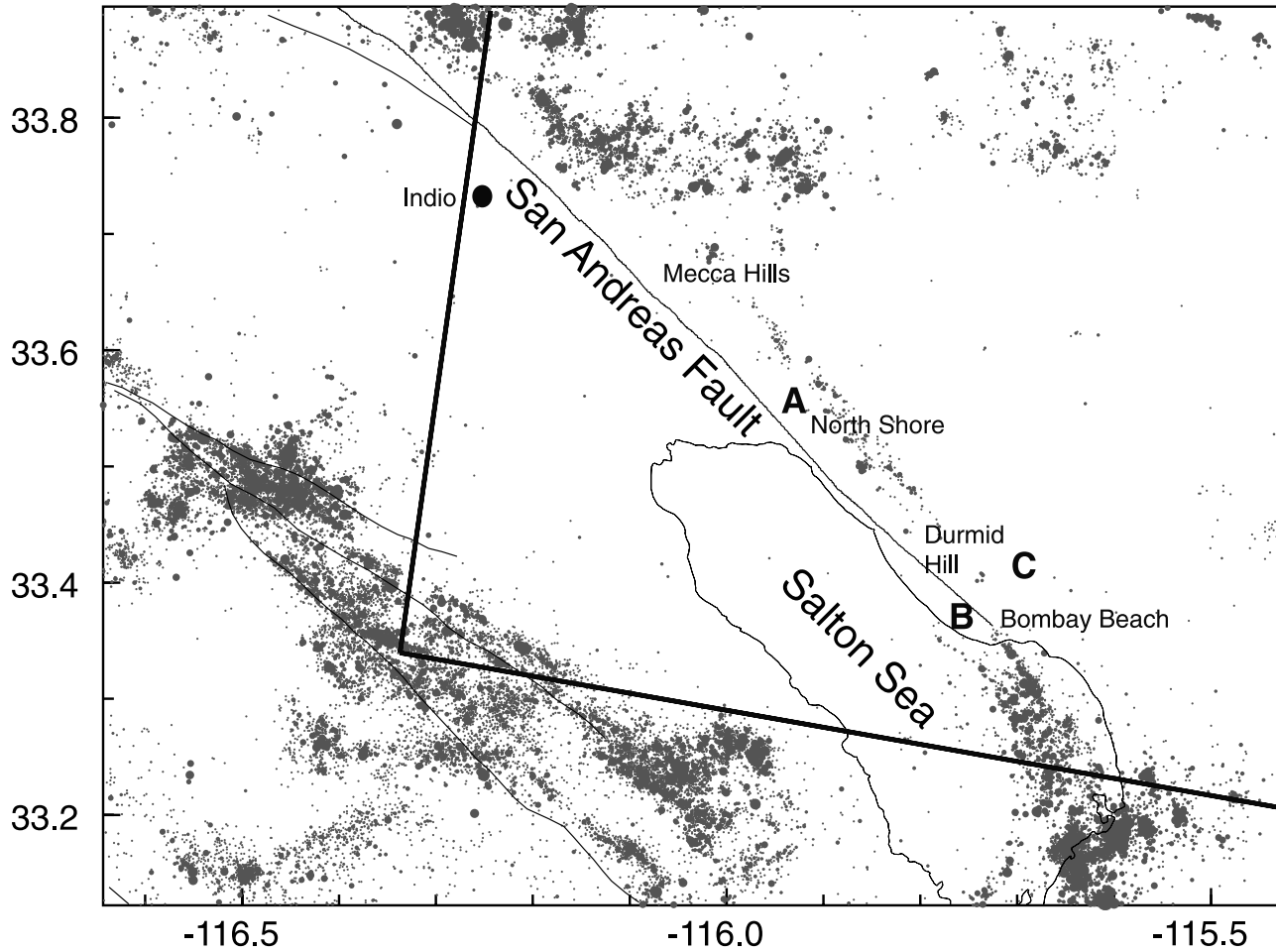


Figure 1. Map view of seismicity in the Coachella Valley. Earthquake locations along the southern San Andreas are offset by ~ 5 km to the northwest of the fault. Locations from Richards-Dinger and Shearer [2000]. Letters are for reference with later figures. Solid lines indicate synthetic aperture radar (SAR) frame from ERS-1/2.

[Louie *et al.*, 1985; Vincent *et al.*, 1998; Sandwell and Agnew, 1999]. The southern San Andreas (Figure 1) has undergone four large slip events between 1000 and 1700 A.D. [Sieh, 1986] and has an earthquake recurrence interval of about 230 years. It has been 300 years since the last major earthquake on this segment, suggesting a significant seismic event along the San Andreas Fault is overdue. The seismicity in this area is low and not on the fault (Figure 1) [Richards-Dinger and Shearer, 2000] and the fault has been known to undergo both continuous creep at 1–2 mm/yr and triggered slip due to earthquakes [Louie *et al.*, 1985; Bilham and Williams, 1985; Rymer *et al.*, 2002]. Thus, it makes for a very interesting region in which to study crustal deformation. Unfortunately, GPS coverage in this region is sparse, so we must rely on Interferometric Synthetic Aperture Radar (InSAR) to determine the small-scale interseismic deformation.

[5] The 9-year archive of SAR data and precise orbital tracking data from the ERS-1 and ERS-2 spacecraft (European Space Agency) was used to recover the slip history of the southern San Andreas Fault (Figure 2). This involved two modes of processing. First, 25 ERS-1/2 pairs having short time spans and moderate baseline lengths (100–300

m) were stacked to recover the topographic phase (thick lines in Figure 2) [Sandwell and Sichoux, 2000]. Then, ERS-1/2 pairs having long time spans (200–3000 days) and short baselines (≤ 186 m; median baseline = 70 m) were used to recover crustal motion. Since this area has more than 2500 m of relief, the accurate development and removal of topographic phase is a critical step in the processing. A comparison with 81 GPS monuments shows the vertical accuracy for the digital elevation model (DEM) using this method is 10 m at 25-m horizontal postings. This topography error maps into less than 13 mm for interferometric baselines shorter than 186 m.

[6] While most of the Salton Sea area is arid and, thus, retains phase coherence over long periods of time, the agricultural areas in the Coachella Valley cause significant decorrelation between SAR images. In the farmland of the Imperial Valley and northwest of the Salton Sea, interferograms formed from available SAR images appear noisy and it is difficult to discern the small-scale deformation across the faults in these areas. Of the sixty interferograms formed from our SAR images, most had high coherence in the region northeast of the fault and showed consistent far-field movement (Figure 3), along with small amounts of fault

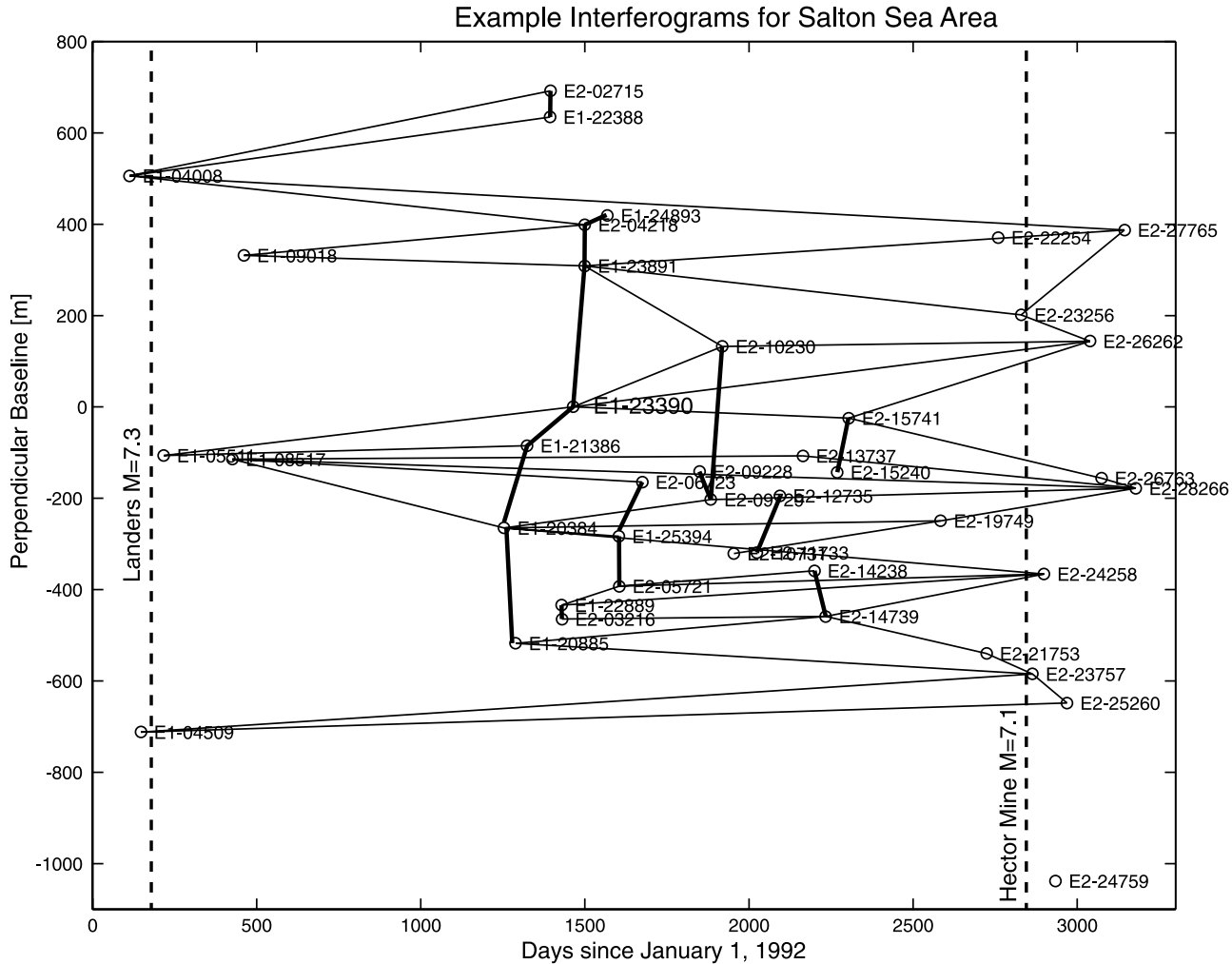


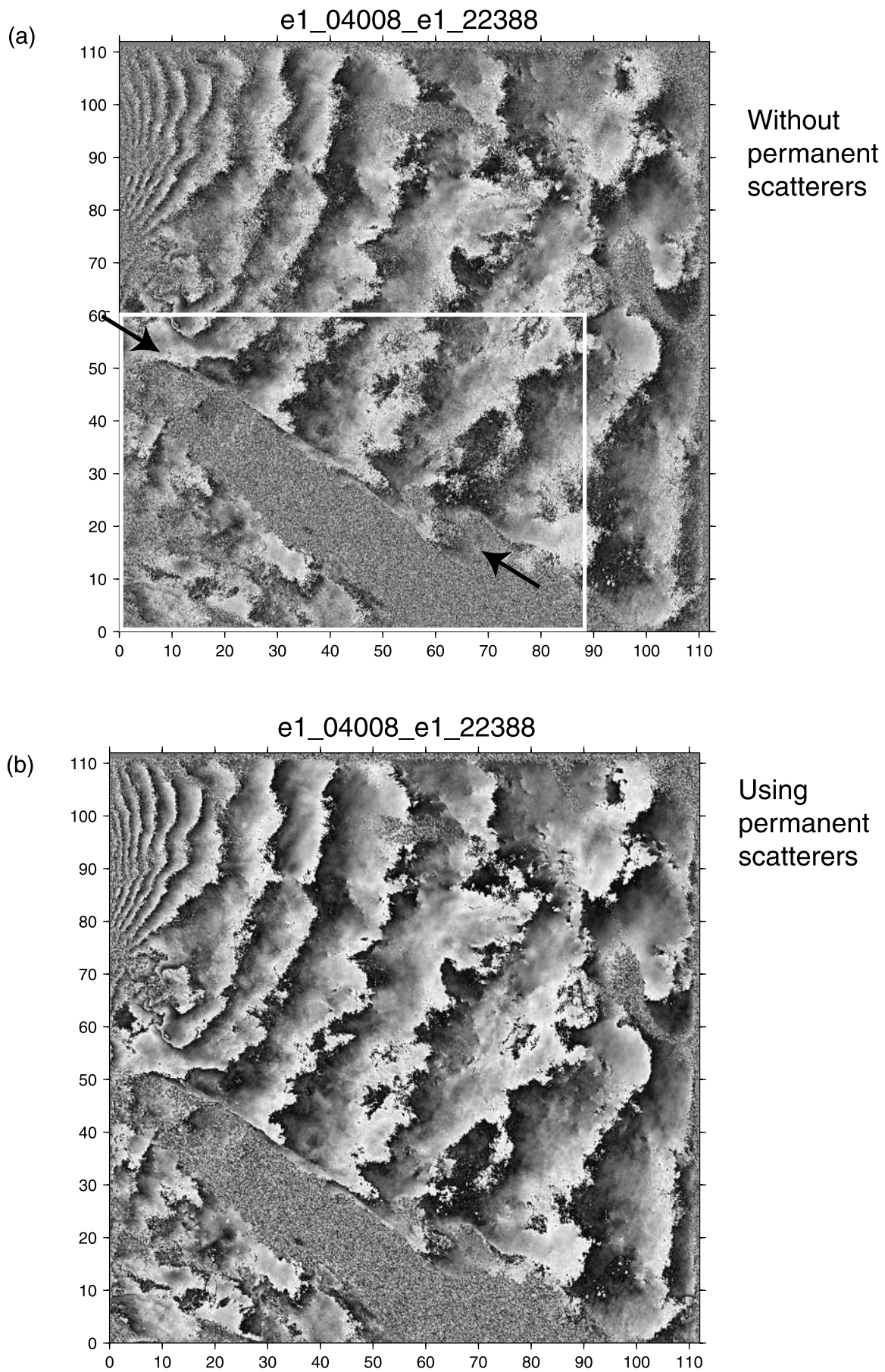
Figure 2. Diagram of available ERS-1 and ERS-2 images of a 120 km × 120 km area containing the southern San Andreas Fault and Salton Sea. These 42 images span almost nine years and include the Landers and Hector Mine ruptures. All images are aligned with the master image (E1_23390) so interferograms can be formed from any pair of images. Phase gradients from pairs with medium baseline difference (50–300 m) and short time difference (<70 days) are stacked to construct a high accuracy digital elevation model (examples shown by thick lines). Pairs with short baseline difference (<186 m) and long time span are used for monitoring small displacements after topographic phase removal (thin lines). For clarity, not all interferogram pairs are shown.

creep (arrows in Figure 3a). However, southwest of the fault, in the Coachella Valley, the interferograms were highly decorrelated and it was difficult to assess the character of motion across the valley. Thus, while one can qualitatively see creep along this section of the San Andreas, the full “picture” of the near-field is muddled by the incoherent farmland.

3. Permanent Scatterers

[7] Decorrelation of the phase in repeat SAR images is caused by cultivation, irrigation, and vegetation growth. However, these agricultural areas also contain isolated reflectors (buildings, roads, drainage channels, etc.) that remain coherent over long periods of time. If these permanent scatterers can be isolated from the generally decorrelated areas [Ferretti *et al.*, 2000, 2001; Haynes, 1999], they

can be used as a data mask (discussed later) or to simulate a dense GPS network. Analysis of the interferograms at these “stable” points can yield the relative motion over time, which can then be used to create a deformation field. Ferretti *et al.* [2001] demonstrated the technique using more than 30 coregistered SAR images in their test regions (Camiore, Milano, and Paris). In their study, after geometric alignment, each amplitude image was scaled using a calibration factor supplied by ESA. The amplitude images were averaged to form the mean of the stack, m_A . They then computed the standard deviation from the mean, σ_A , to form the amplitude dispersion index, D_A , at each pixel, such that $D_A = \frac{\sigma_A}{m_A}$. Points of low amplitude dispersion ($D_A < 0.25$) were labeled “permanent scatterers.” From this subset of points, Ferretti *et al.* [2001] jointly estimated the digital elevation model (DEM) errors, line-of-sight (LOS) velocities, and linear atmospheric contributions [see Ferretti *et*



al., 2001 for details]. This secondary analysis involved an iterative, least-squares procedure to effectively unwrap the phase and isolate the time series of crustal deformation.

[8] Our analysis of 37 SAR images along the Southern San Andreas Fault initially followed the approach of Ferretti *et al.* [2000] to identify the permanent scatterers. However, we deviated from their technique when using this information. We began by calculating the amplitude dispersion from the stack of SLC images, but rather than use a calibration factor from ESA, we calculated the average calibration factor for each image using the ratio of the amplitude of each image (mean of all pixels) to the mean amplitude of the entire set. Each SAR image was divided by this calibration factor to equalize the brightness between images, and we calculated the scattering amplitude, s , which is the inverse of the amplitude dispersion, D_A (Figure 4). Stable areas with low dispersion have a high scattering amplitude and, thus, have higher phase stability, while bodies of water, such as the Salton Sea in Figure 4, have zero phase stability and so the scattering function, s^2 , is close to zero.

[9] Interferogram formation typically involves the following steps: cross-multiplication of the aligned single-look complex SAR images; removal of all known phase effects due to Earth curvature, topography, orbital geometry, etc.; and multi-look (boxcar or Gaussian) filtering of the real and imaginary parts of the interferogram to boost the signal-to-noise ratio [Massonnet and Feigl, 1998; Rosen *et al.*, 2000]. Rather than isolate the permanent scatterers using a threshold and treat them as an array of known points [Ferretti *et al.*, 2001], we modified the filtering step using the scattering function at each pixel (s_j^2) (Figure 4). We multiplied the real and imaginary parts of each pixel by s_j^2 and then filtered each component with a Gaussian filter oriented approximately along the fault (N47.5°W), such that the width of the filter along the fault, σ_{par} ($\lambda_{0.5} = 285$ m), is greater than the width of the filter perpendicular to the fault, σ_{perp} ($\lambda_{0.5} = 84$ m). Pixels with high s -values are given more “confidence” and weighted more than those with high dispersion (low s -value) prior to spatial filtering of the interferogram, C ,

$$\langle C(\mathbf{x}) \rangle = \langle R(\mathbf{x}) \rangle + i \langle I(\mathbf{x}) \rangle$$

where $\langle \rangle$ denotes the Gaussian convolution filter. This weighting boosts both the real and imaginary parts of the amplitude of stable areas prior to filtering, but does not alter the phase of the pixel, since the phase is: $\phi = \tan^{-1}\left(\frac{\langle s^2 \text{Im}(C) \rangle}{\langle s^2 \text{Re}(C) \rangle}\right)$.

[10] Figure 3 illustrates the qualitative improvement in phase recovery by using the weighting and filtering method versus using normal interferometric methods. This interferogram spans 3.5 years and includes the Landers earthquake. Figure 3a was formed using the standard interferometric techniques with a nearly isotropic Gaussian filter ($\lambda_{0.5} = 84$ m azimuth, $\lambda_{0.5} = 105$ m ground range; see Sandwell and Price [1998]). The fringe edges are rough and highly pixellated, and the Coachella Valley creates a decorrelated

barrier between the fringes of the northeast section and those in the southwest region. Figure 3b shows the resultant interferogram after weighting the amplitude components by the square of the scattering index and filtering with the Gaussian filter oriented along the fault. The fringes in this interferogram are much more highly defined and areas within the Coachella Valley are more coherent than before. In the northwest region of the valley, the fringe pattern is almost continuous across the valley, with only minor pixellation.

[11] To look more quantitatively at the effects of the weighting, we determined the correlation between two SAR images used in a four-year interferogram spanning the interseismic period (July 1995 through June 1999). Although the coherence measurement may seem to be a more relevant measure of the impact of the permanent scatterers technique, we wanted to examine the difference on a pixel-by-pixel basis, so we found the correlation of the image pair for both our weighted permanent scatterers technique (γ_{WPS}) and the standard technique (γ_{std}). The correlation value is defined as simply $\gamma = \frac{\langle A_{12} \rangle}{\sqrt{\langle A_1 \rangle \langle A_2 \rangle}}$, where A_1 , A_2 , and A_{12} are the amplitudes of the reference image, the repeat image, and the interferogram between the two, respectively.

[12] The difference between these values, $\gamma_{WPS} - \gamma_{std}$, for the four-year interferogram is shown in Figure 5. The top image (Figure 5a) shows the distribution of correlation improvement and demonstrates a positive correlation difference (improvement) for the weighting technique in most regions. This is supported by the histogram of the region (Figure 5b) which shows a normal distribution, offset by ~ 0.01 . The vast majority of pixels were either unchanged or experienced an improvement in the correlation due to the scatterers (mean = ~ 0.014 , median = ~ 0.015). Areas of complete decorrelation with no permanent scatterers within the footprint of the convolution will not be improved using this technique and also areas of perfect correlation cannot be improved. Therefore, we expect the most improvement from this permanent scatterer weighting and filtering method will come from areas where the correlation is marginal (~ 0.2). In highly decorrelated areas, it may be preferable to use only the permanent scatterer points and discard the other data (similar to Ferretti *et al.* [2001]). Further experimentation is needed in areas of varying correlation to determine the optimum masking, weighting, and filtering technique that will maximize the correlation of the data while still maintaining a useful spatial resolution along the fault.

4. Stacking Interferograms

[13] Interferometric “signal” is composed of topographic height variations, surface deformation, orbit errors, and signal delay variability within the image due to the atmosphere. To isolate the creep signal, we first removed the topographic phase from each interferogram. The surface

Figure 3. (opposite) (a) Interferogram of the southern San Andreas fault zone (box) processed using the standard method. Indio is in the western part of the image and the Salton Sea cuts toward the southeast. This interferogram spans 3.5 years and includes deformation from the 1992 Landers event (fringes in upper left). Each fringe corresponds to 28 mm of deformation. Creep can be seen along the San Andreas Fault (black arrows). (b) Interferogram processed from the same images, but using permanent scatterers to weight the pixels during multilook averaging.

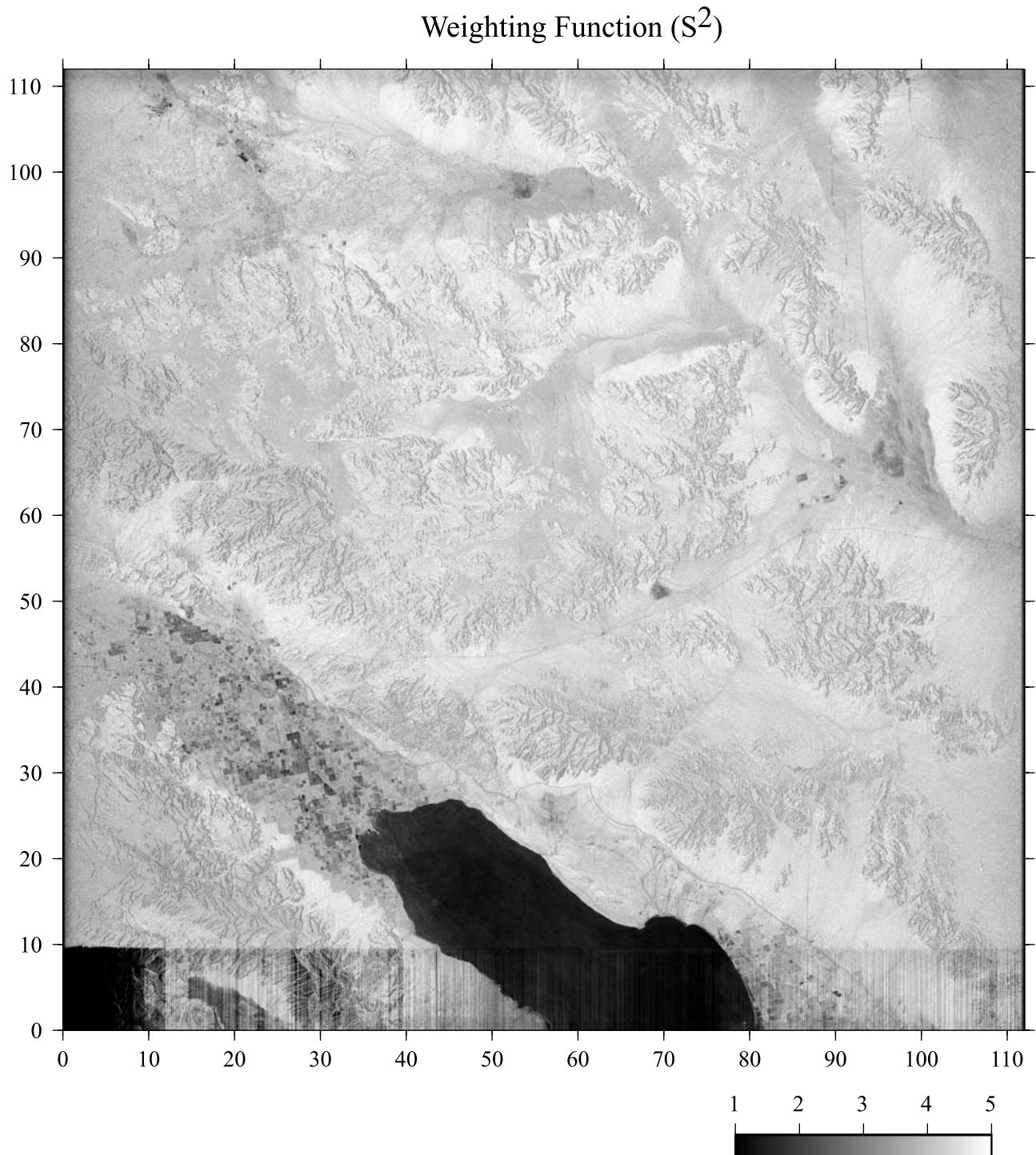
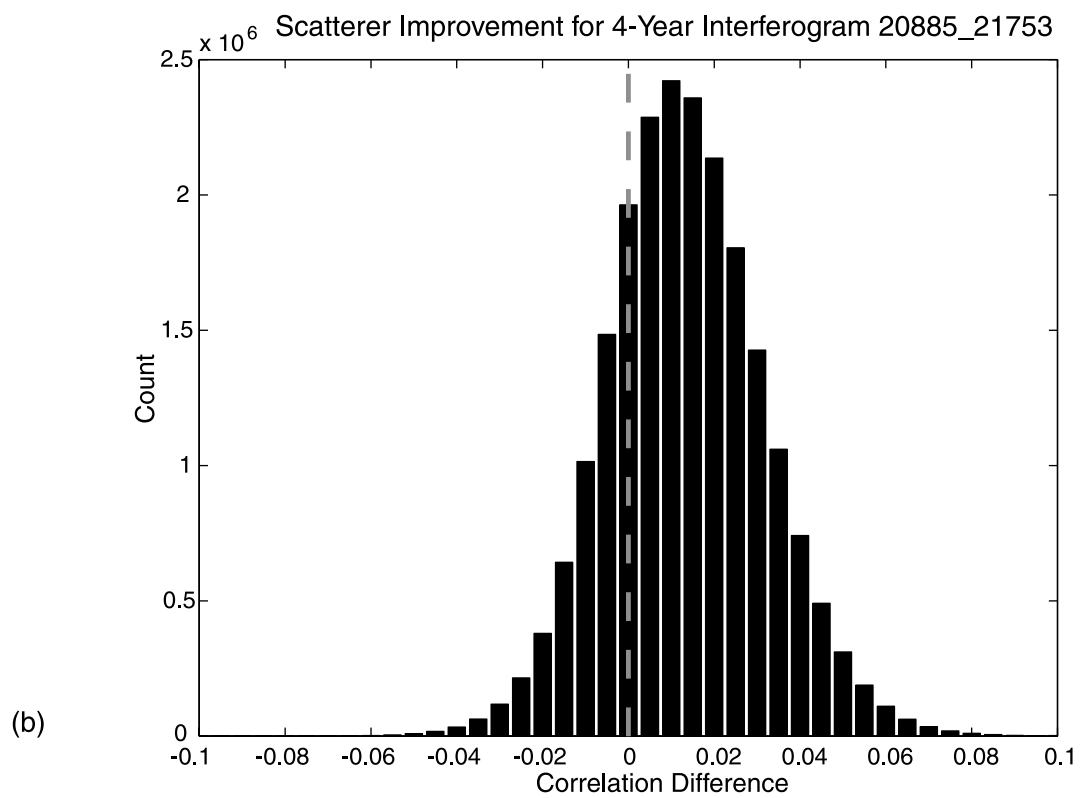
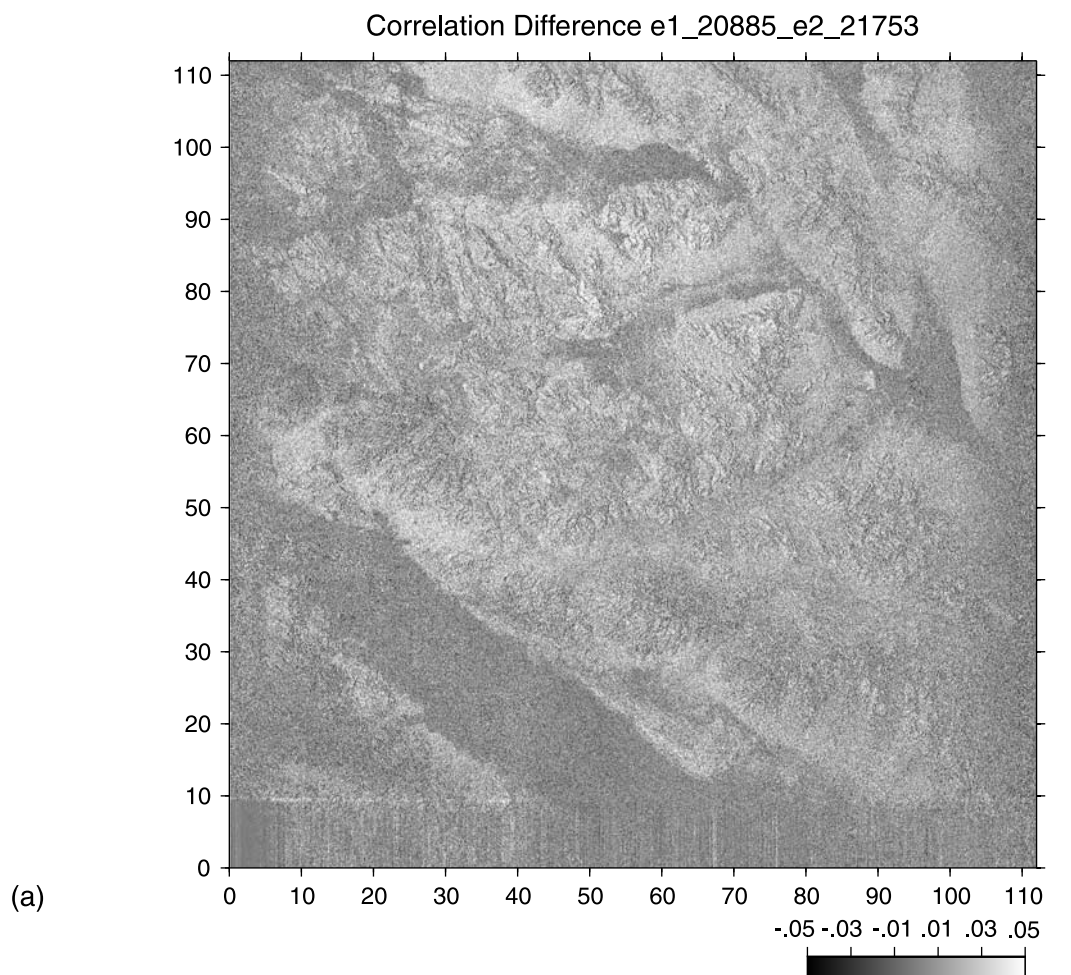


Figure 4. Permanent scatterer weights (s^2) from a stack of 37 descending ERS images. Bright regions are “stable” and considered highly reliable, while black regions experience sporadic, random motion (plowing of fields, overlay effects of mountains) and are used as masks in the weighting process, as described in the text.

Figure 5. (opposite) (a) Difference between the correlation of a 4-year interferometric pair (E1_20885 to E2_21753) using the permanent scatterer weights versus using the standard method. This demonstrates a positive correlation difference (improvement) for the weighting technique in most regions. (b) Histogram of Figure 5a, showing a normal distribution, offset by ~ 0.01 , mean = ~ 0.014 , median = ~ 0.015 .



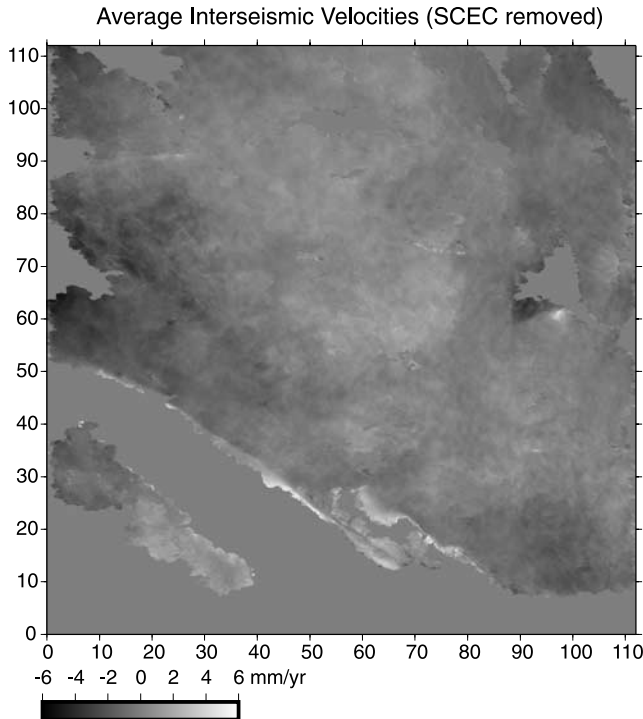


Figure 6. Average LOS interseismic creep velocities for 1993–1999. The far-field velocity model and the orbit error model have been removed from each interferogram prior to stacking.

deformation is composed of both long-wavelength (far-field) motion and short-wavelength (near-field) creep. We estimated the far-field motion using the Southern California Earthquake Center (SCEC) velocity model (SCEC Crustal Dynamics Working Group, 1999, available at http://www.scec.org/group_e/release.v2) for the region (based on continuous GPS stations) and interpolated for velocities between stations. After removing this long-wavelength signal, our resultant signal should be comprised of orbit error, tropospheric error, and creep. For each of the sixty interferograms, we unwrapped the phase and attempted to manually bridge gaps in the data. Since the orbit error is nearly a plane over a 100 km distance [Massonnet and Feigl, 1998], we removed a plane estimating the best fit linear gradient across the unwrapped phase data from each phase array. Most of these unwrapped interferograms showed evidence for fault creep, but the line-of-sight signal was very small and it was difficult to obtain reliable measurements from a single interferogram. Assuming the tropospheric errors are random, stacking multiple interferograms should reduce this noise, leaving the creep signal. Figure 6 shows the unwrapped interseismic interferogram stack with the SCEC velocity model and orbit error estimate removed. The resultant signal is the average over seven years of data (1993–1999) and shows creep along the northwest and southeastern sections of the fault region.

5. Results

[14] To look for evidence of triggered slip along this segment of the San Andreas Fault due to the Landers and

Hector Mine earthquakes, we divided the set of interferograms into three different time periods (Table 1): Landers (1992–1996), Interseismic (1993–1999), and Hector Mine (1997–2000). Twelve interferograms spanned more than one time period, so they were not used in the stacks. The SCEC velocity model was added back into each stack before modeling.

[15] For the Landers stack, we used four interferograms encompassing both the earthquake and three and a half years of postseismic motion (22 April 1992 to 10 February

Table 1. Atmospheric Error Statistics for All Interferograms, With Each Interferogram Categorized Into Its Corresponding Time Category^a

Image	Time Span	Number of Data Used	Mean, mm	σ , mm
Interseismic Stack	1.00	16036454	-0.39	0.98
e1_08517_e1_20384	2.27	15661458	1.38	8.53
e1_08517_e1_23390	2.84	15839799	4.50	9.64
e1_08517_e2_09228	3.90	15949683	1.71	7.86
e1_08517_e2_13737	4.76	15917989	2.16	8.13
e1_08517_e2_15240	5.05	15882854	1.24	6.25
e1_08517_e2_15741	5.15	15726075	5.90	10.23
e1_08517_e2_19749	5.91	15418444	-0.84	9.49
e1_09018_e1_23891	2.84	15797617	2.08	8.28
e1_09018_e2_04218	2.85	14556996	3.16	8.04
e1_20384_e1_25394	0.95	16007701	1.65	7.91
e1_20384_e2_09729	1.73	15972479	0.12	5.44
e1_20384_e2_19749	3.64	15958108	-1.07	6.84
e1_20885_e2_21753	3.93	15970992	-3.59	12.94
e1_22889_e2_05721	0.48	16011506	0.99	7.96
e1_23390_e2_13737	1.92	15904598	-1.23	7.79
e1_23390_e2_15741	2.30	15996066	3.74	7.37
e1_23891_e2_23256	3.64	15794977	0.24	8.38
e1_25394_e2_10731	0.96	16013454	-1.71	6.78
e2_03216_e2_14739	2.20	15973252	1.18	6.15
e2_03216_e2_21753	3.55	15891411	-1.80	8.01
e2_05721_e2_14238	1.63	15974680	0.70	9.88
e2_09729_e2_15240	1.05	15978842	0.12	6.59
e2_10731_e2_11733	0.19	16030262	-0.11	8.50
e2_10731_e2_14238	0.67	16008501	-1.68	8.38
e2_10731_e2_19749	1.73	15962245	-0.92	4.94
e2_11733_e2_14238	0.48	16007444	-1.68	9.97
e2_11733_e2_19749	1.53	15972968	-0.90	8.16
e2_13737_e2_15741	0.38	15946210	5.89	12.09
e2_14238_e2_19749	1.05	15934429	0.61	7.52
e2_14739_e2_21753	1.34	15898121	-3.40	10.77
Hector Stack	1.00	16000194	-1.05	5.22
e2_11733_e2_24258	2.40	15899373	-3.23	8.97
e2_13737_e2_28266	2.78	15841896	-0.49	8.69
e2_14238_e2_24258	1.92	15941333	-1.45	5.90
e2_14739_e2_24258	1.82	15762022	-0.32	7.61
e2_15240_e2_26763	2.21	15787982	7.33	11.32
e2_15741_e2_26763	2.11	15506748	1.34	11.22
e2_19749_e2_24258	0.86	15869345	-3.56	10.03
e2_19749_e2_28266	1.63	15885884	0.80	6.15
e2_21753_e2_23757	0.38	15973780	0.91	8.88
e2_23256_e2_26262	0.58	15928559	-1.09	8.72
e2_23256_e2_27765	0.86	15507135	5.50	12.64
e2_23757_e2_25260	0.29	15964596	-2.18	6.52
Landers Stack	1.00	14578153	-0.87	4.77
e1_04008_e1_22388	3.51	14371067	2.52	6.82
e1_04008_e2_02715	3.52	14252541	1.49	7.43
e1_04008_e2_04218	3.80	14335058	-1.35	13.45
e1_04509_e1_20885	3.13	14023711	-0.13	12.91
Median	1.92	15814939	0.12	8.13

^aThe standard deviation of the atmospheric signal for most of the interferograms is <10 mm.

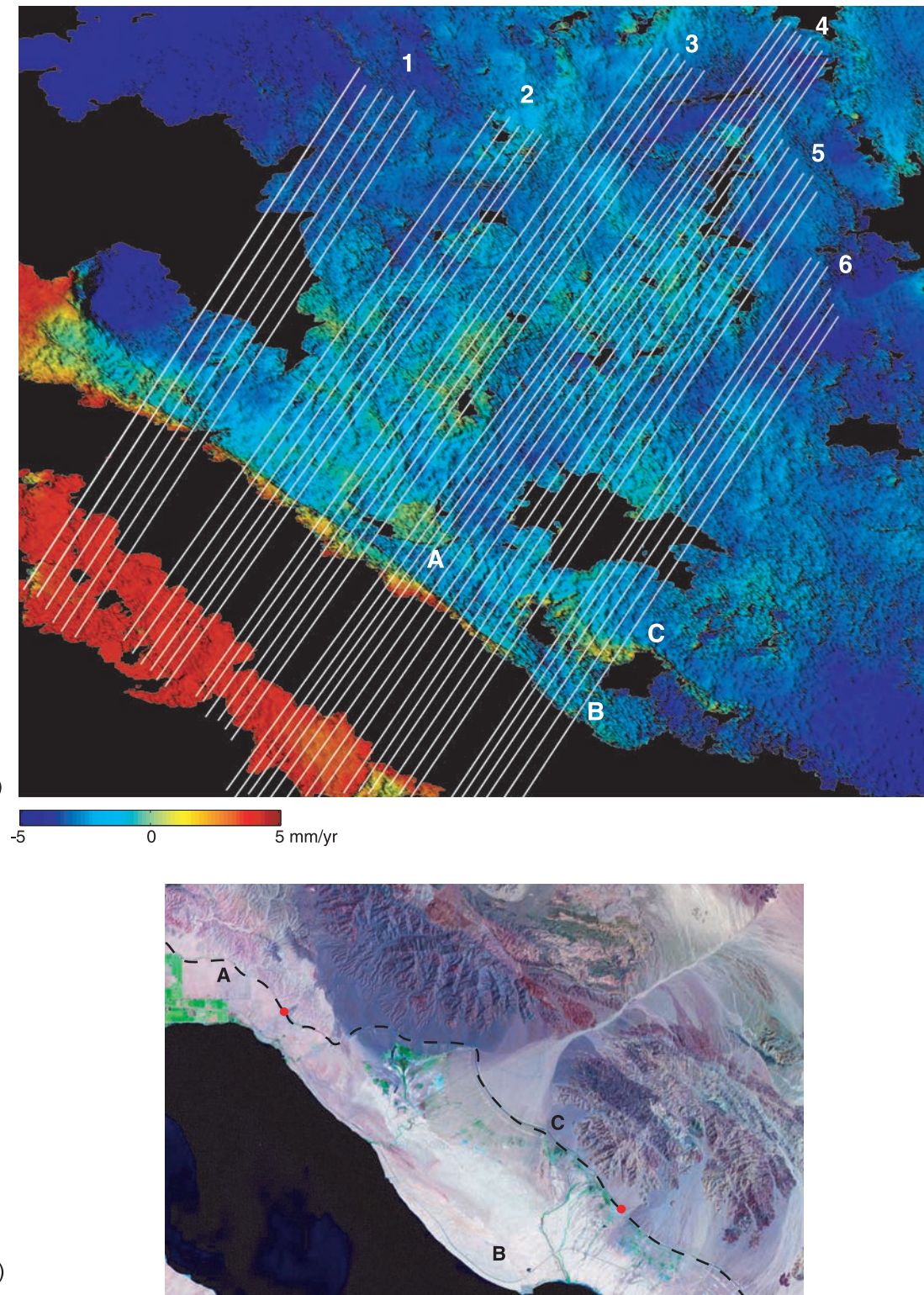


Figure 7. (a) Unwrapped line of sight (LOS) displacement for a stack of interferograms encompassing the Landers event. Red is 5 mm/yr LOS motion (away from the satellite); blue is -5 mm/yr LOS (motion toward the satellite). Black areas indicate regions without good point scatterers (high dispersion) and are masked out. White lines correspond to the profiles used in modeling the fault behavior (Figures 8–10). Thirty-eight profiles are used to estimate the locking depth of the shallow portion of the fault. (b) Aerial photography of sections 5 and 6 near the Bombay Beach/Durmid Hill region of the Salton Sea. Pixel resolution is 64 m and covers a 40 km × 32 km area. The Coachella Canal is shown as a thick dashed line. Red dots signify the endpoints of the unlined section of the canal. Image courtesy of the U.S. Geological Survey.

1996). The average line-of-sight (LOS) velocity during this 3.5-year period is shown in Figure 7a, with red indicating 5 mm/yr line-of-sight (LOS) motion (away from the satellite or northwest) and blue indicating –5 mm/yr LOS (toward the satellite or southeast). The sharp jump across the fault indicates that some sections of the fault experienced creep during the Landers quake, while other regions along the fault appear to be locked to the surface. To look more quantitatively at the spatial distribution of slip along the fault, we extracted 38 profiles across the length of the fault region (numbered lines in Figure 7a). Because the creep appears to vary in magnitude from northwest to southeast, we divided the profiles into six groups. These profile groups were used to model the fault movement at depth.

[16] Since our displacement measurements are in the radar line-of-sight (LOS) reference, we must convert to fault-parallel horizontal motion prior to modeling. If we define ϕ to be the azimuth of the southern San Andreas ($\sim 312.5^\circ$ [Bilham and Williams, 1985]), θ as the incidence angle (23° for ERS in the center of the SAR frame), and α as the azimuth of the line-of-sight vector (103° for descending ERS tracks), we can write the LOS displacement for a descending pass as:

$$[\Delta LOS_d] = [-\sin \alpha \sin \theta \quad -\cos \alpha \sin \theta \quad -\cos \theta] \begin{bmatrix} \Delta x \\ \Delta y \\ \Delta z \end{bmatrix}.$$

[17] If we then assume a vertical fault plane with purely horizontal strike-slip motion, Δs , we can rewrite the x and y components as:

$$\begin{aligned} \Delta x &= \Delta s \sin \phi \\ \Delta y &= \Delta s \cos \phi \end{aligned}$$

and the relationship between the line-of-sight and fault-parallel motion becomes:

$$\Delta LOS_d = \Delta s(-\sin \alpha \sin \theta \sin \phi - \cos \alpha \sin \theta \cos \phi) \approx 0.3401 \Delta s.$$

[18] Care must be taken when converting from LOS to strike-slip values using this assumption of purely horizontal motion, as any vertical motion would be converted to strike-slip displacement. For example, one mm of subsidence would map into ~ 2.7 mm NW motion, while one mm of uplift would map into 2.7 mm of SE motion. Field observations along the southern San Andreas, however, have shown evidence of purely dextral motion with only minimal (~ 1 mm) vertical slip in scattered areas [Rymer, 2000; Rymer et al., 2002] so our assumption should be valid for this region.

[19] Figures 8–10 show the resultant profile groups for the Landers, Interseismic, and Hector stacks, respectively. The Landers stack (Figure 8) reveals fault creep in every group over the 3.5-year period except for group 6 at the southernmost end near Durmid Hill. Durmid Hill is a 4 km wide and 20 km long hill at the southern terminus of the San Andreas Fault (B in Figure 7). Its formation has been attributed to transpression along the San Andreas [Bilham and Williams, 1985; Sylvester et al., 1993] and leveling data has shown that Durmid Hill is growing aseismically at a rate of 1–2 mm/yr [Sylvester et al., 1993]. Previous creep meter studies have revealed episodic creep near Durmid of 1–3 mm/yr from 1967–1984 [Bilham and Williams, 1985] and triggered creep in 1992 from the Joshua Tree (1.5 + 1 mm) and Landers (3.9 mm) events [Bodin et al., 1994]. Although a prominent creep signal is not seen in our profiles, the scatter of the points near the fault makes it difficult to isolate a signal of this magnitude in the Durmid Hill region, so we do not rule out the possibility of very small creep in this area.

[20] The average interseismic velocity from 1993 to 1999 is shown in Figure 9. A sharp jump in velocities at the fault in group 1 (far northwest) indicates creep of 3–5 mm/yr LOS (9–15 mm/yr horizontal) in this region, but it is not as apparent in groups 2 and 3. Toward the middle of the region (group 4), there is evidence of ~ 6 mm/yr LOS (18 mm/yr horizontal) of surface slip, continuing southeast through group 5 and the Desert Beach/North Shore region (A in Figure 7). The far southeast segment of the fault (group 6), between Durmid Hill and Bombay Beach (B in Figure 7), does not show distinct signs of creep.

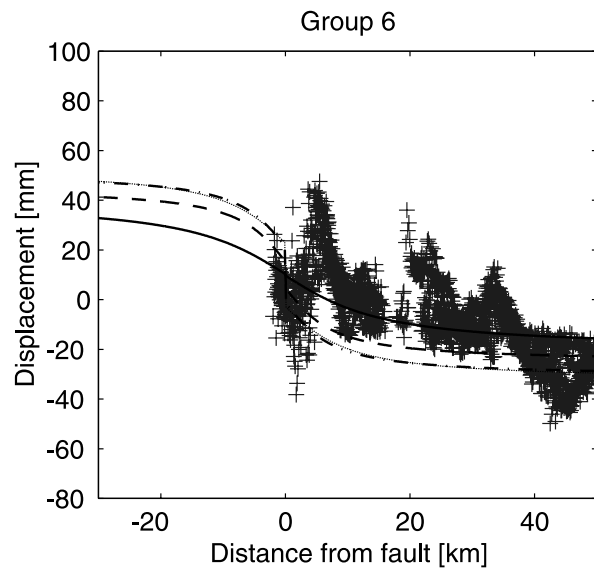
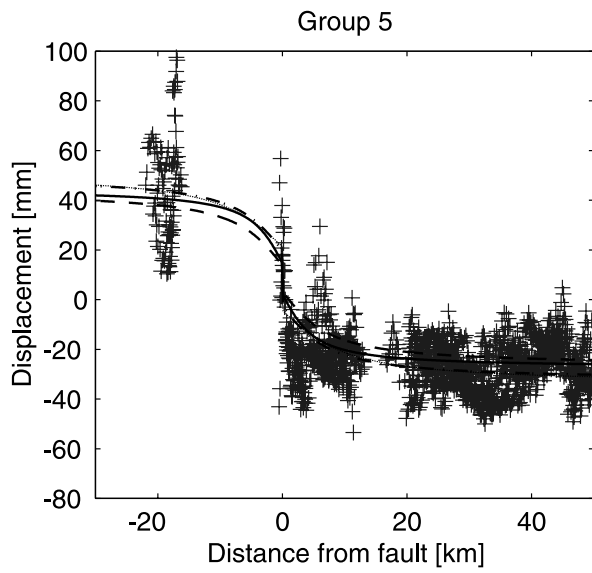
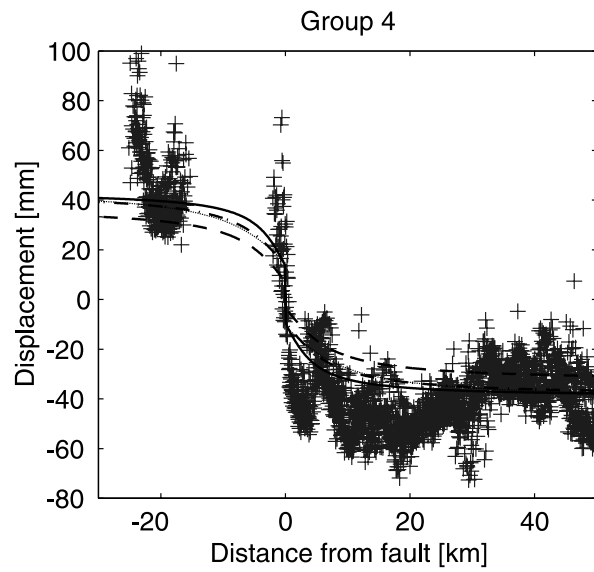
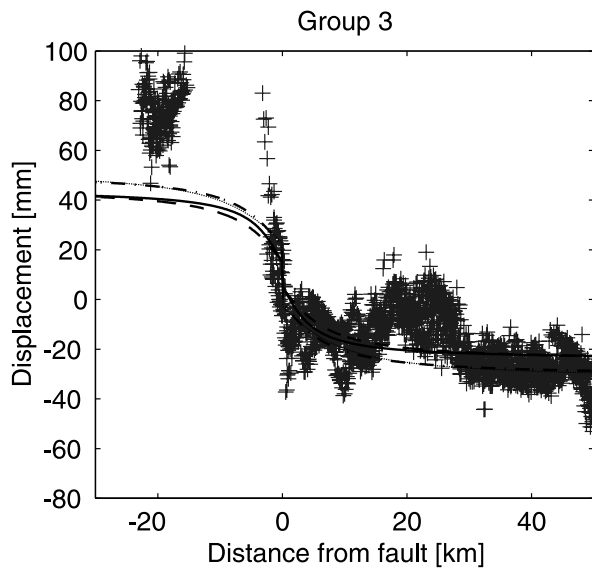
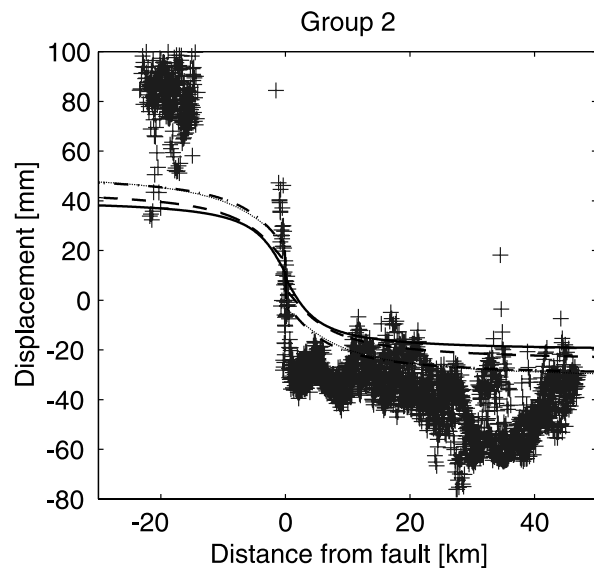
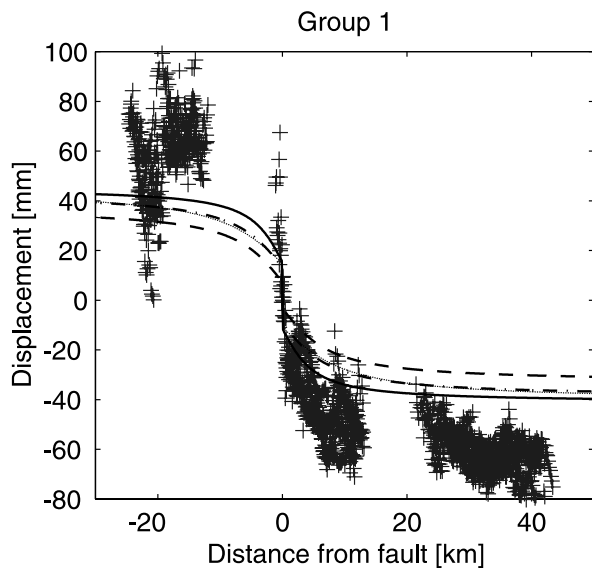
[21] The profiles for the Hector Mine stack yielded similar results (Figure 10) to the interseismic stack. We used 12 interferograms (Table 1) spanning three years (19 July 1997 to 16 September 2000), including one year of postseismic data. Groups 1, 4, and 5 showed 4–6 mm/yr LOS (12–18 mm/yr horizontal) of creep, with a reduced rate for section 2 and no creep for groups 3 and 6.

[22] To determine the amount of triggered slip due to the Landers event, we subtracted the average interseismic displacement from the Landers stack for the 3.5 year time-period. The result is shown in Figure 11 and ranges from –20 to 30 mm LOS. Near the fault, the displacement varies from a 50 mm LOS (14.7 cm horizontal) slip difference in the northwest (arrow Figure 11) to nearly zero in the southeast near Durmid Hill. For the main segment of our survey region, triggered slip due to the Landers earthquake amounts to 15–35 mm LOS (4.5–10 cm horizontal) over the three and a half year period.

[23] To see if there is a similar pattern for the Hector Mine earthquake, we subtracted the average interseismic velocities for a three-year period from our Hector stack. This gives an approximation of the slip due to Hector Mine during 1999–2000. The results (Figure 12) reveal over a

Figure 8. (opposite) Horizontal displacement over 3.5 years for profile groups from the stack of 4 interferograms used in Figure 7 (Landers event), compared with preliminary models. Zero distance corresponds to the mapped fault location. Solid lines are “best fit” models with 17 mm/yr strike-slip applied to an elastic half-space having a free-slip plane below depth D and slip from the surface to a depth d . For comparison, dashed line is $D = 6$, $d = 0.9$, dash-dot line is $D = 8$, $d = 2.9$, and dotted line is $D = 6$, $d = 1.9$. “Bad” points (decorrelated areas) are defined by a scattering amplitude of <2 and are masked out.

Landers Stack



Interseismic Stack

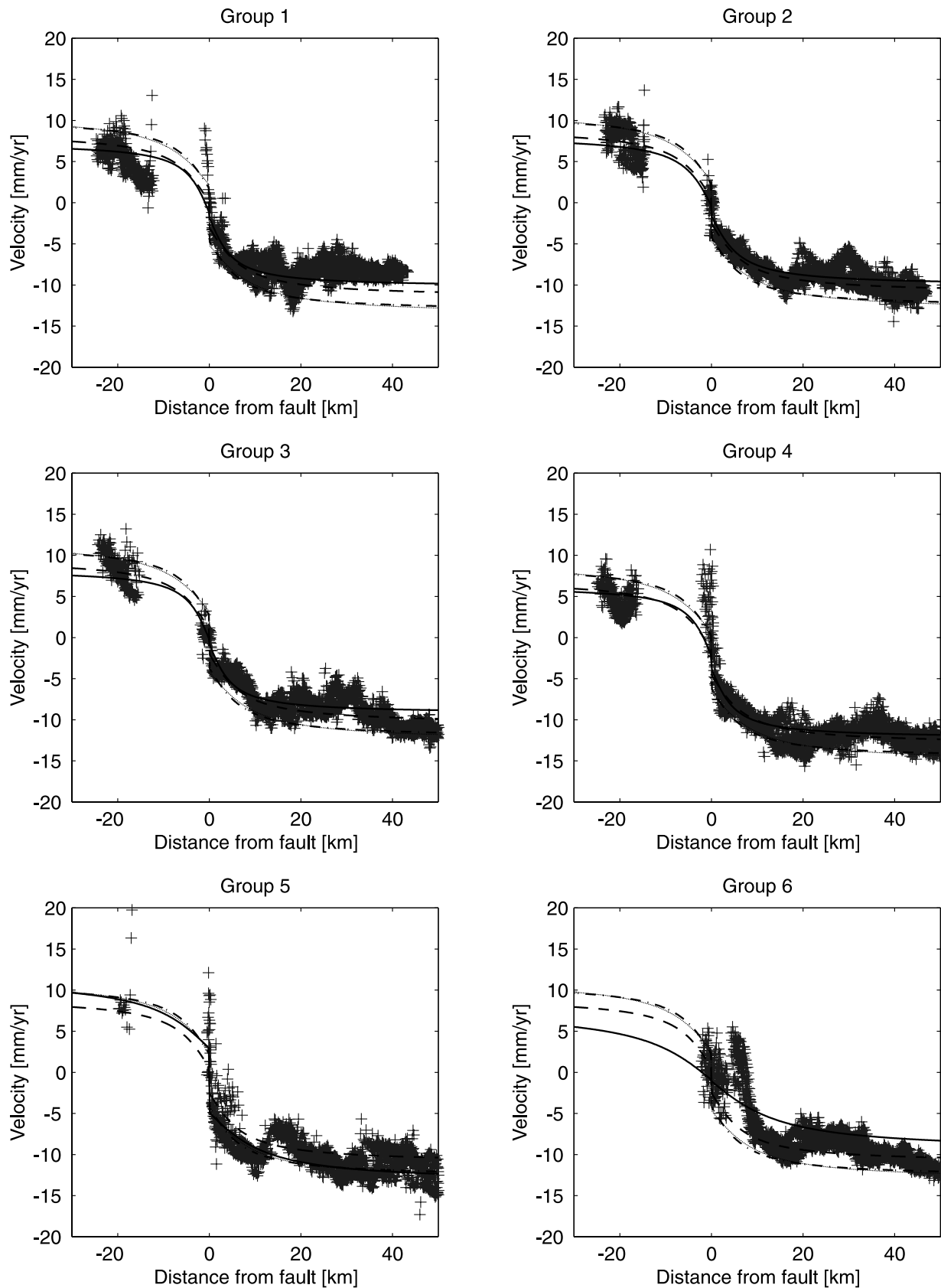


Figure 9. Same as Figure 8, but for the stack of 28 interseismic interferograms, time averaged over 1993–1999.

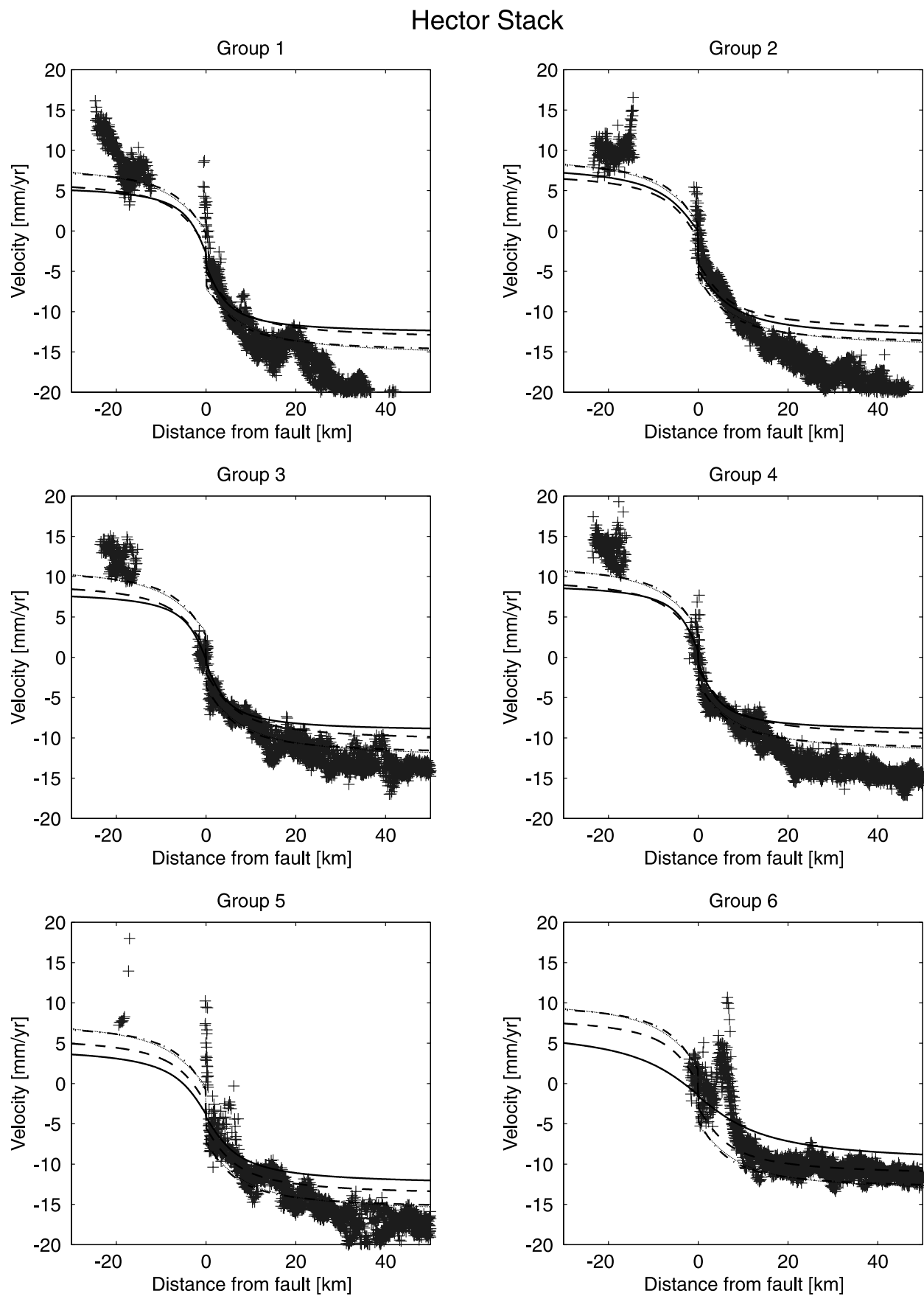


Figure 10. Same as Figure 9, but for the stack of 12 Hector Mine interferograms, time averaged over three years.

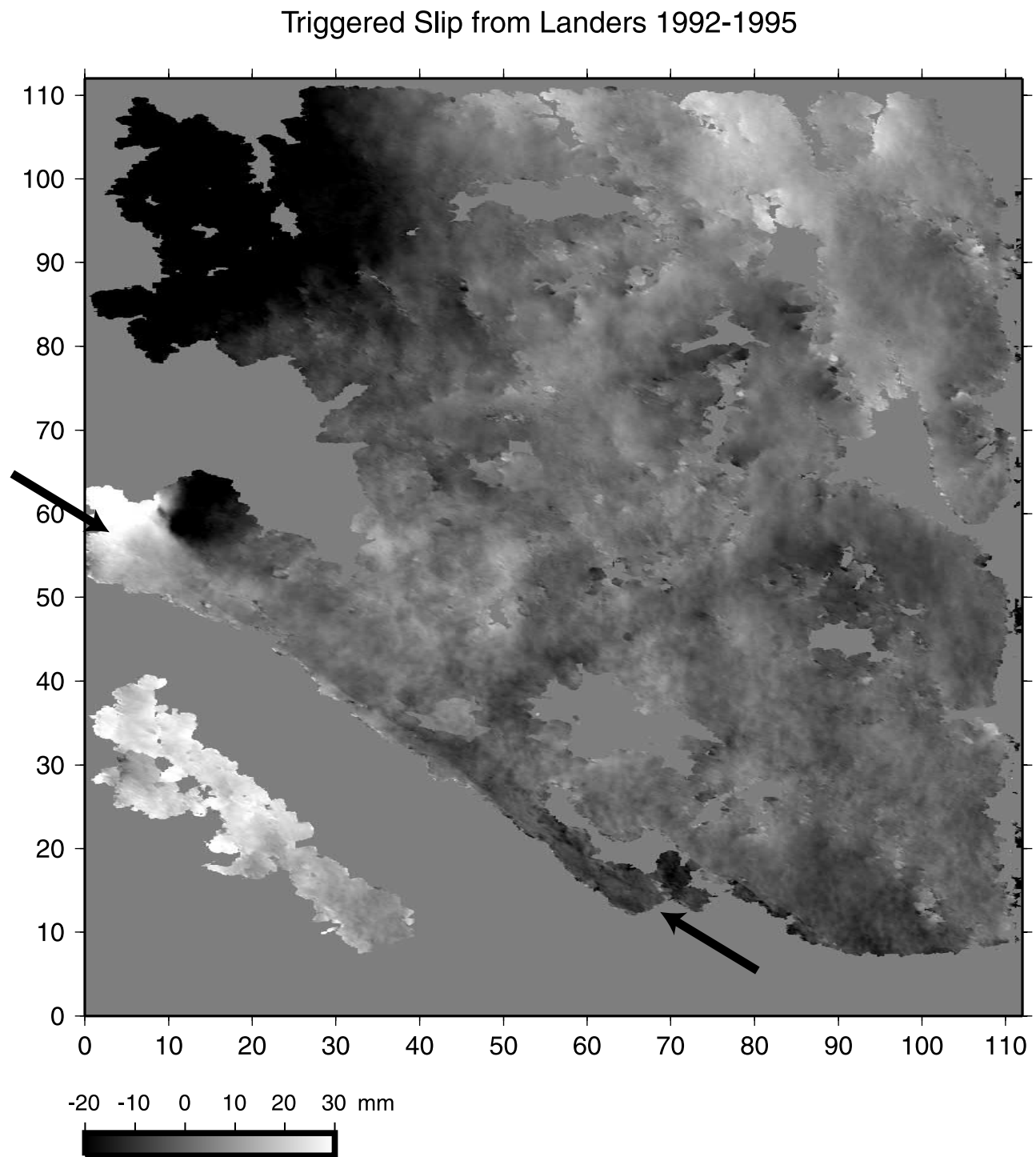


Figure 11. Triggered slip from the Landers earthquake for 1992–1995. Image was formed by removing the average interseismic signal for the 3.5-year time span from the Landers stack. Triggered slip ranges from 5 cm LOS (14.7 cm horizontal) in the northwest (arrow) to zero in the southeast.

centimeter of LOS motion across the entire region, but very little near-field triggered creep across the fault.

6. Fault Models

[24] We adopted the fault model originally proposed by *Weertman* [1964] and subsequently developed by *Savage*

and *Lisowski* [1993] to determine the distribution of slip with depth for this section of the San Andreas. The model consists of two plates sliding past each other with a far-field plate velocity of V . The simplest model has a fault that slips freely between minus infinity and a deep locking depth of D (Figure 13). Our data show evidence for shallow creep between the surface of the Earth and some shallow locking

Triggered Slip from Hector Mine 1999-2000

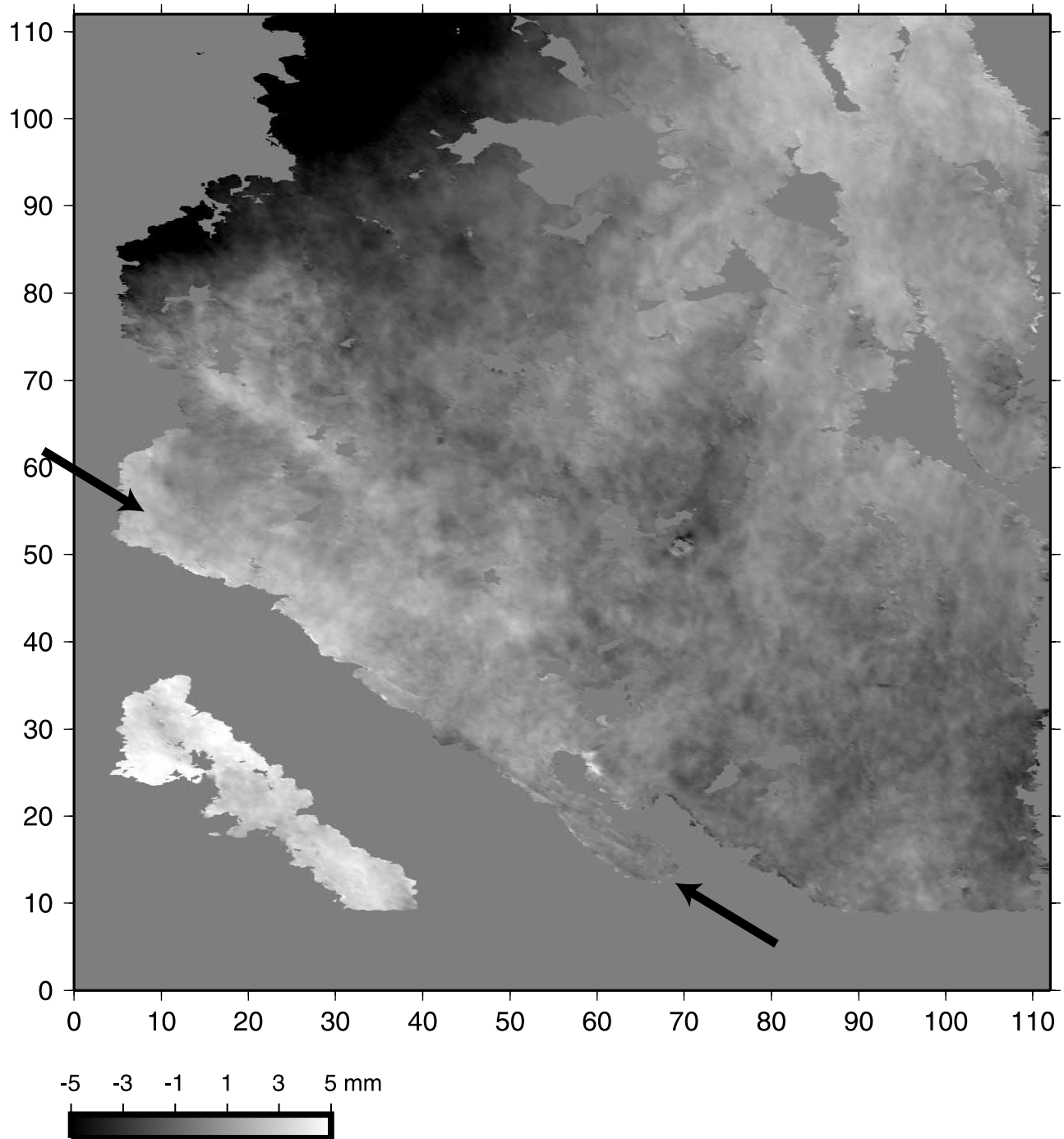


Figure 12. Same as Figure 11, but for the Hector Mine earthquake and one year of postseismic signal. Values are much smaller than for Landers and the far-field effect is more noticeable.

depth d . We use the model of *Savage and Lisowski* [1993] to evaluate this shallow creep signature. In their model, shallow creep occurs when the far-field tectonic stress plus the local stress concentration due to the deep fault slip exceeds the fault strength. Fault strength depends on the coefficient of friction (~ 0.85 for most rocks [Byerlee, 1978]) times the normal stress, where normal stress has a component due to lithostatic pressure plus an unknown

tectonic component of normal stress. The details of the model are found in the work of *Savage and Lisowski* [1993]. The unknown parameters are the deep locking depth D and the tectonic normal stress. If there is no shallow creep, the displacement follows a smooth arctangent function (Figure 13, solid curve, surface locked). If there is combined shallow slip and deep slip, the displacement field will have a local abrupt transition superimposed on the

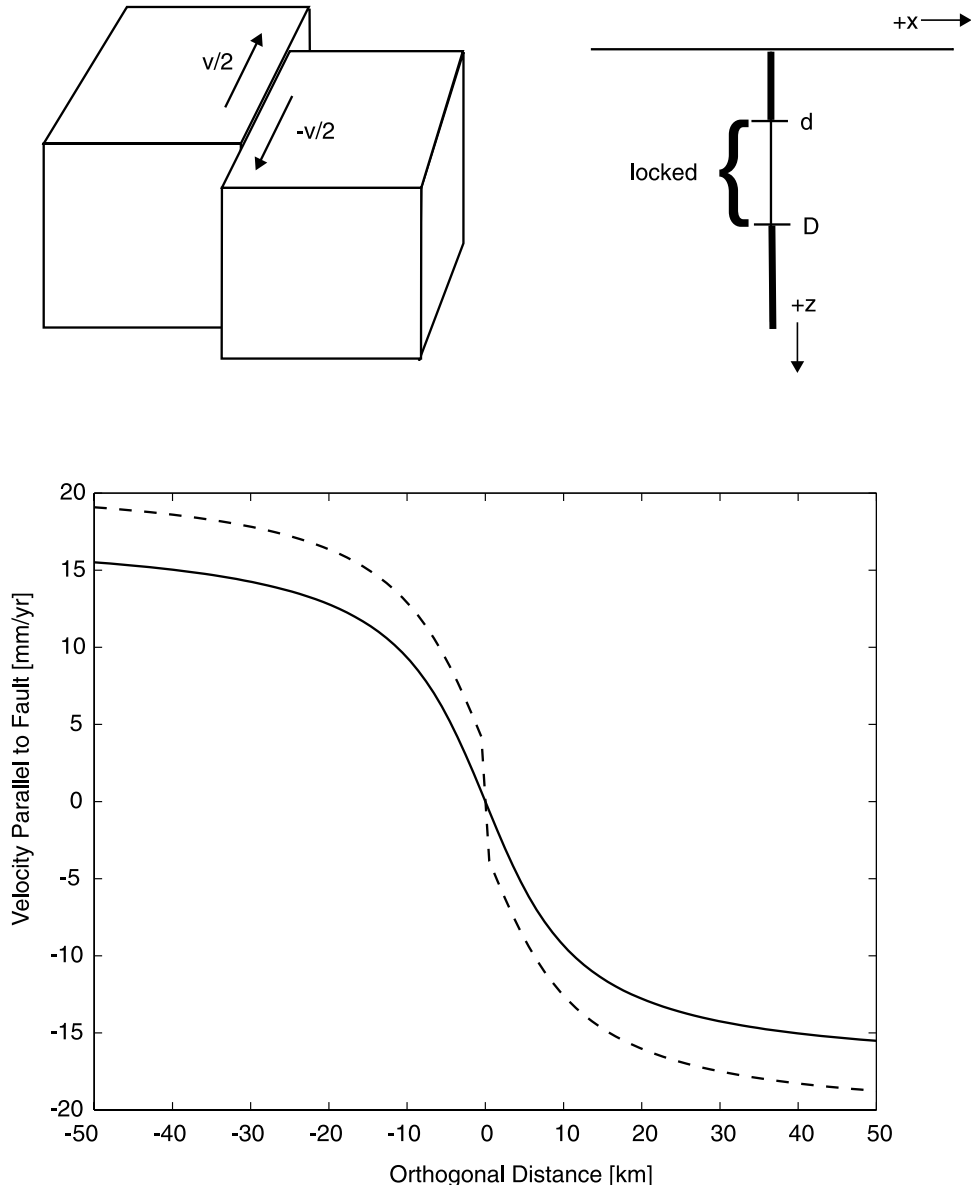


Figure 13. Simple elastic dislocation model. (top) A right-lateral, strike-slip fault in which two blocks slide past each other with velocity v . (bottom) The resultant deformation signature across the fault if (solid line) the fault is locked from the surface to depth D and slips freely below D , and if (dashed line) the fault is locked only between d and D . Note, this is a zero-stress boundary condition on the unlocked areas of the fault plane so displacement is continuous everywhere.

broad displacement field (Figure 13, dashed curve, surface creep).

[25] We varied the deep locking depth (4 to 12 km) and the tectonic normal stress (−10 to 50 MPa) to find the corresponding creeping depths. Previous estimates of the secular slip rate for the southern San Andreas Fault vary from $V = 12$ mm/yr [Wdowinski *et al.*, 2001] to $V = 26$ mm/yr [Bennett *et al.*, 1996; *Working Group on California Earthquake Probabilities*, 1995]. Using velocities from continuous GPS stations in the Coachella Valley and surrounding areas (SCEC Crustal Dynamics Working Group, 1999, available at http://www.scedc-scec.org/group_e/release.v2), we estimated the far-field velocity as 17 mm/yr and ran our modeling program

using deep slip rates of both 17 mm/yr and 26 mm/yr. Using the profiles across the fault during the interseismic phase (Figure 9), we estimated the slip rate on the surface at the fault trace to be 12 mm/yr, and then calculated the stress rate for each $D-d$ pair from Savage and Lisowski [1993] equation A13. We determined the surface velocity caused by the slip on the upper segment of the fault and calculated the root mean square (RMS) misfit to the geodetic measurements (plus an unknown constant). To account for the large number of far-field measurements versus the near-field data, we weighted the misfit between the model and observations such that the misfit is equal to 1 at the fault and falls off by $\frac{1}{\sqrt{|x|}}$ with distance, x , from the fault. We tested the effect of varying both the surface

RMS Misfit - Interseismic Stack

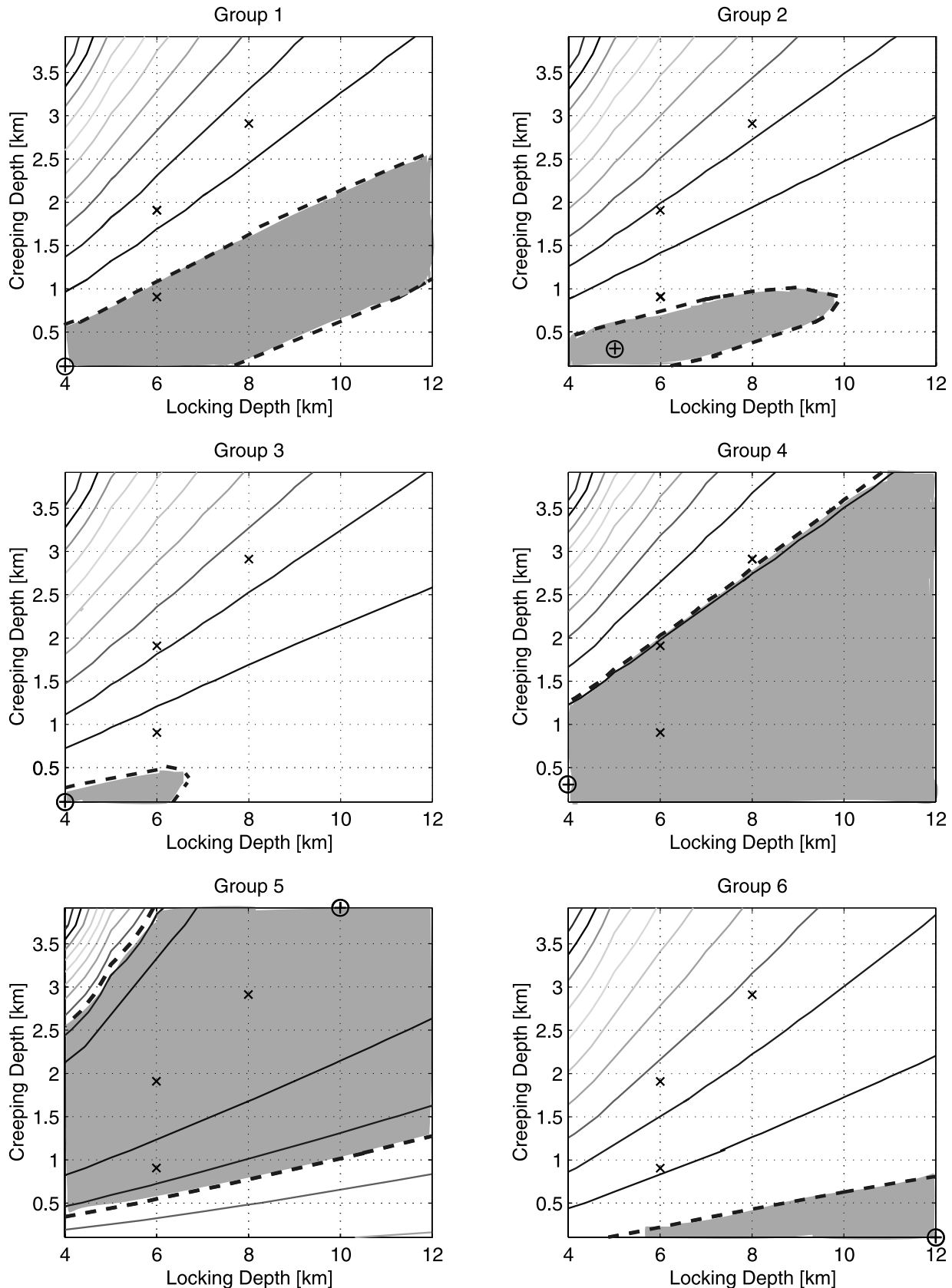


Figure 14. RMS values for weighted misfit between observations and models for the interseismic stack. Circled cross indicates the minimum misfit parameters; crosses indicate other model values plotted in Figure 9. Shaded areas are minimum misfit plus 10%.

Table 2. Comparison of Creep Rates for the Southern San Andreas Fault From 1967 to 2000

	Bilham and Williams	Louie et al.	Rymer et al.	This Paper			
	Triggered 1968/1978, mm	Average 1967–1984, mm/yr	Average 1967–1984, mm/yr	Triggered 1992/1999, mm	Interseismic (1993–1999), mm/yr		
	LOS	Horizontal	Segment				
Indio	0/0	2	1.4–1.8	0–10/–	3–5	9–15	1
Canal	0/0	0	0–3	0/0	0–2	0–6	2
Mecca Hills	9.5/4	3	1.7–3.1	0–20/0–10	0–2	0–6	3
North Shore	~0/0	0	0	0/0	5–7	15–20	4
Durmid	5/2.5	2	–	0–2/~0	5–7	15–20	5
					~0	~0	6

slip rate value (5–20 mm/yr) and the coefficient of friction (0.85, 0.4) and found the differences in misfit values negligible.

[26] Figure 14 shows the interseismic RMS misfit between the GPS-derived velocities and the forward models for the range of locking depths and corresponding creeping depths using $V = 17$ mm/yr. The minimum misfit for each region is plotted as a circled cross, and its corresponding forward model is shown in Figure 9 (solid line). The dashed contour line in Figure 14 represents the minimum RMS value plus 10% and illustrates that there is a wide range of “reasonable” models for our data (shaded areas). For comparison, Figures 8–10 show the forward models for $[D = 6, d = 0.9]$ (dashed line), $[D = 8, d = 2.9]$ (dash-dot line), and $[D = 6, d = 1.9]$ (dotted line). These parameter values are marked with an “x” in Figure 14. Note that, for the two models with a locking depth of 6 km, altering the creeping depth changes the model significantly. However, the models for $D = 6, d \sim 2$ (dotted) and $D = 8, D \sim 3$ (dash-dot) are virtually identical, illustrating the tradeoff between locking depth and creeping depth values and the need for other sources of information (seismic, etc.) to constrain the locking depth of the fault in order to define the creeping depth. Once the locking depth is well constrained, it becomes easier to determine the most reasonable creeping depth using this model. Unfortunately, for this section of the southern San Andreas, seismicity is extremely low, so determining the locking depth is difficult. *Wdowinski et al.* [2001] give a value of 3.8 ± 3.3 km for the Coachella Valley, based on the relocations by *Richards-Dinger and Shearer* [2000], while *Hauksson and Jones* [2000] show the majority of seismic events in the Coachella Valley occur ≤ 6 km depth, with a few as deep as 10–15 km.

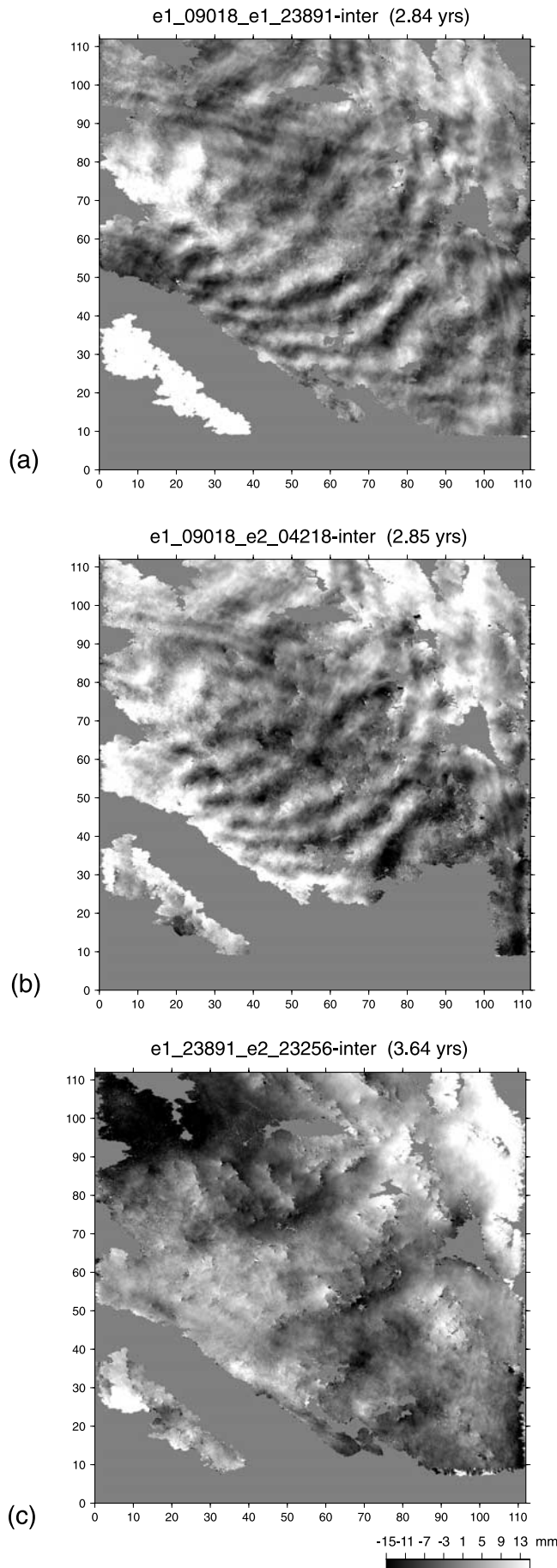
7. Discussion

[27] The sequence of interferogram stacks reveals a diffuse secular strain buildup that is punctuated by localized fault creep. With the exception of the far southeast section near Durmid Hill, this entire segment of the San Andreas Fault appears to creep over the time interval encompassing the 1992 Landers earthquake. Slip is continuous for more than 60 km from Durmid Hill to Indio and the line-of-sight component of right-lateral offset ranges from 12 to 35 mm (which maps into 3.5–10 cm of strike-slip motion) for the 3.5 year period. This triggered slip following the earthquake relieves much of the added stress that *Stein et al.* [1992] and

King et al. [1994] predicted for the Coachella segment of the San Andreas due to the Landers event. Their Coulomb stress change model predicted that 7 cm of slip would be required to compensate for the added stresses on the fault due to Landers, with another 30 cm required to relieve the long-term stress change (equivalent to a $M = 5.7$ earthquake). Although they concede that these numbers may be overestimates, there is still a clear indication that a significant amount of the stress load related to Landers has been released aseismically along the fault over the last decade. Although this shallow creep reduces the seismic moment on the slipping section, it is important to note that stress is transferred to the deeper locked segment, bringing it closer to failure.

[28] From 1993 until mid-1999, aseismic slip was mainly confined to two regions: northwest of Indio and between North Shore (A in Figure 7a) and Durmid Hill. The time history of the deformation during this period is not well determined from interferometry, although creep meters and strainmeters along the fault suggest that this creep is episodic [Bodin et al., 1994]. Following the 1999 Hector Mine earthquake, the near-field slip pattern does not alter much, though we do see increased slip during 1999–2000 of over a centimeter LOS in the far-field. To the southeast of Durmid Hill, toward Bombay Beach, there appears to be no sign of fault creep over the past decade, but a small signal may be hidden in our data.

[29] Previous studies of the southern San Andreas by *Louie et al.* [1985] and *Bilham and Williams* [1985] covering 1967–1984 have indicated much lower values (0–3 mm/yr) of time-averaged creep for the southern San Andreas. Bilham and Williams also noticed an apparent relationship between the observed creep rate and the strike of the fault, with creep occurring along sections of similar strike (N47.5W). This pattern was also seen in the geologic observations of triggered slip following the Landers [Rymer, 2000] and Hector Mine [Rymer et al., 2002] earthquakes. However, our results indicate that after 1992, the reverse pattern is true, with the fault appearing locked in the previously creeping sections and vice versa (see Table 2 for comparison). Since all of the sections of the southern San Andreas appear to have undergone triggered slip due to the Landers quake, the apparent switch between locking and creeping sections after the event could indicate an equalization of stress along the fault over the entire time span (1967–2000). The magnitude of slip across the fault in our study is 3–4 times the earlier ones obtained by creep meters and could reflect



either an underestimation of creep rates using creep meters versus geodetic means (as has been reported by *Lisowski and Prescott* [1981] and *Langbein et al.* [1983]) or a longer-term increase in the average creep rate since the Landers earthquake. Geologically derived slip measurements are also generally underestimates of slip since the distributed shear across the entire fault zone is not always manifest on the cracks [*Bodin et al.*, 1994].

[30] All of the stacks show evidence of an apparent LOS velocity increase of ~ 5 mm/yr northeast of the fault in group 6 (C in Figure 7). The motion occurs along a 2–5 km wide strip just downstream of the intersection of Salt Creek and the Coachella Canal (along dashed line in Figure 7b). A LOS increase translates to either northwest relative motion (horizontal component) or deflation (vertical component). The deformation occurs off the fault, suggesting a largely vertical component of motion. If this signal were due to erosion from stream flow, we would see decorrelation in this area of the interferograms, similar to the black areas southwest of point C in Figure 7a. But a regional slumping or long-term deflation would cause a coherent relative increase in the LOS signal on the northeast side of the fault, similar to that in Figure 7a.

[31] There are multiple possibilities as to the cause of this subsidence. The Coachella Valley has a delicate water balance and the Water District consistently pumps groundwater to supply the fields and houses in the region. Thus, the most likely cause of ground subsidence is a groundwater extraction rate that exceeds the resupply rate. However, an interesting correlation exists between the area of subsidence and the leaking section of the Coachella Canal.

[32] The Coachella Canal is 122 miles long and is a major branch of the All-American Canal system. Its turnout is 37 miles downstream from Imperial Dam. When the canal was constructed in 1948, it was Earth-lined except for the last 38 miles, from Lake Cahuilla southward to near North Shore (A in Figure 7), which were concrete-lined. In 1980, to save an estimated 132,000 acre-feet of water annually which had been lost through seepage (14% of its capacity), the first 49 miles of the Coachella Branch were replaced with a 48-mile long concrete-lined canal (Coachella Valley Water District, 2001, available at <http://www.cvwvd.org/water&ccv.htm>). This leaves almost 35 miles of unlined canal along the Salton Sea between Niland and North Shore (dashed line between red dots in Figure 7b), which loses an estimated 9,000 acre-feet of water per year (U.S. Bureau of Reclamation, 2001, available at <http://dataweb.usbr.gov/html/coachella.html>). This unlined section follows the same route as the upslope origination of the signal seen in the interferometry, thus

Figure 15. (opposite) Residual interferograms displaying atmospheric noise. The interseismic stack and any ramps (orbit error) have been removed from interferograms (a) e1_09018_e1_23891, (b) e1_09018_e2_04218, and (c) e1_23891_e2_23256. Residuals range from -15 to 15 mm, regardless of interferogram time span. Comparison indicates the large rippling in Figures 15a and 15b is due to image e1_09018. This signal is not correlated with topography and is indicative of gravity waves in the troposphere.

corroborating that the almost 6 mm/yr vertical motion is caused by a net loss of groundwater near the canal, perhaps due to mining.

8. Atmospheric Effects

[33] As discussed earlier, once the topographic phase and orbit errors are removed from an interferogram, the resultant signal is composed of the deformation signal and the atmospheric delay. To qualitatively assess the nature of atmospheric delay in this region, we assume that the deformation signal is a secular trend that is common to all interferograms (i.e., pairs of SAR images) while the atmospheric water vapor signal is mostly uncorrelated among individual SAR images. This is not always the case since, as we have seen, creep can be episodic and triggered slip can occur after nearby earthquakes, causing deformation signals that occur in only a few interferograms. However, for our analysis of the atmospheric effects, we use only interseismic interferograms, remove the average interseismic signals, and focus on signals greater than ~ 10 km from the fault.

[34] There are two types of signals due to atmospheric water vapor [Hanssen, 2001]. The first is due to turbulent mixing in the atmosphere and is largely uncorrelated with topography. The second signal is caused by a change in the vertical stratification of the troposphere between the lowest and highest elevations in the area. This signal is highly correlated with topography. The turbulent mixing in the neutral part of the atmosphere is predominantly from effects of the water vapor in the troposphere [Hanssen, 2001] and the phase delay is independent of radar frequency, rendering multi-wavelength measurements (such as those used to correct GPS ionospheric errors) useless. Relative humidity changes of 20% can lead to 100 mm of error in deformation maps, independent of baseline parameters [Zebker *et al.*, 1997]. Thus, the average of many interferograms is needed to minimize tropospheric effects and isolate the deformation signal. In many cases, the turbulent mixing signal appears as ripples in the image due to gravity waves. Gravity (or internal) waves are oscillations in the atmosphere which can occur as weather fronts are formed, from flow instability in the jet stream, as air flows over mountains, and as large-scale clouds form. They are responsible for mountain lee waves and clear air turbulence and have been the topic of numerous SAR studies [e.g., Chunchuzov *et al.*, 2000; Vachon *et al.*, 1995]. Atmospheric gravity waves usually cause local variations of <1 cm in interferograms, and typically have wavelengths of 3–10 kilometers [Vachon *et al.*, 1994; Mattar *et al.*, 1997].

[35] The tropospheric signal for an interferogram can be isolated from the secular deformation signal by subtracting the stacked signal (i.e., scaled by the time interval between the reference and repeat SAR acquisitions). Previously, only ERS-1 to ERS-2 tandem interferograms (i.e., 1-day time interval) were used to isolate tropospheric effects, in order to minimize temporal decorrelation and to exclude any deformation signal [Hanssen, 2001]. Here we wish to investigate the optimal sampling strategy needed to separate the deformation and atmospheric signals using an actual set of interferograms. We assume that stacking N interferograms reduces the noise in the stacked image by $\frac{1}{\sqrt{N}}$. Thus, we can

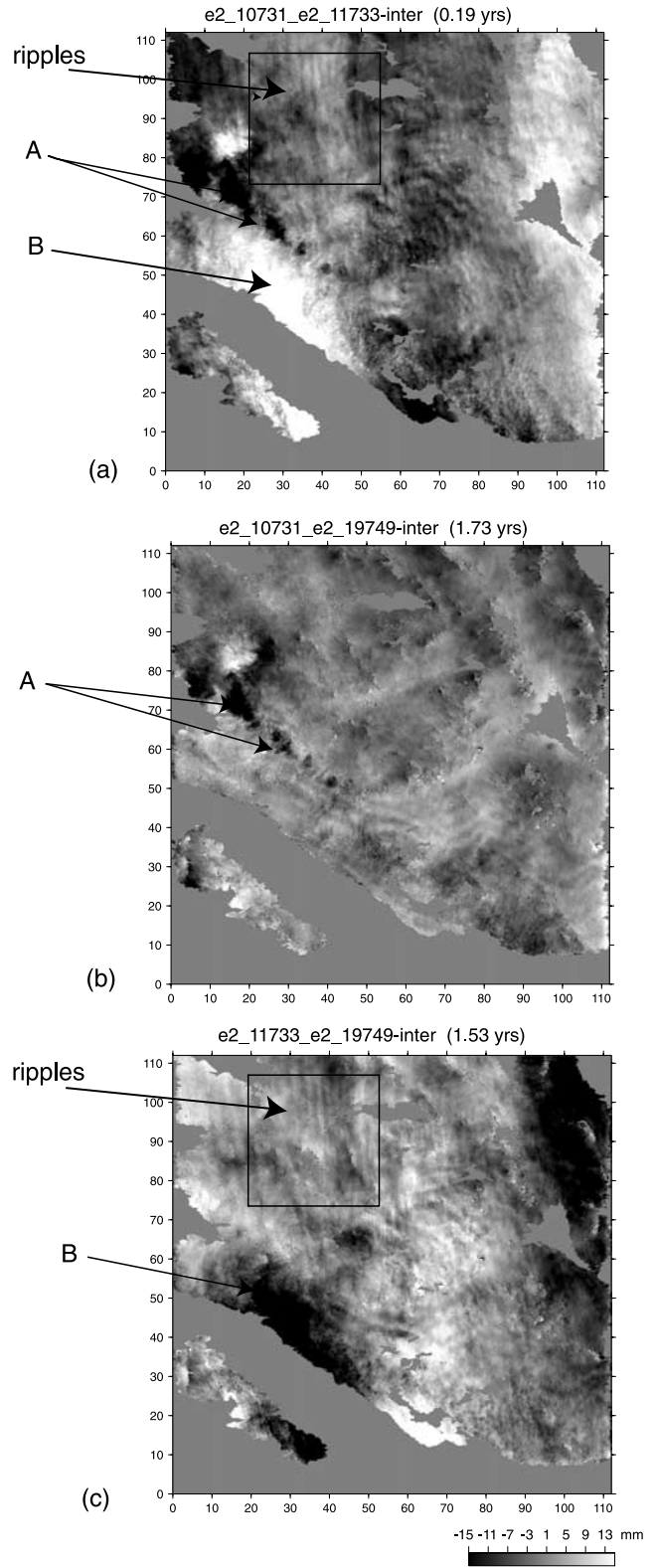


Figure 16. Same as Figure 15, but for (a) $e2_10731_e2_11733$, (b) $e2_10731_e2_19749$, and (c) $e2_11733_e2_19749$. Comparison of images shows atmospheric “ripples” in $e2_11733$ and large “blotches” in the western regions of $e2_10731$ (labeled A). $e2_19749$ does not show any predominant error patterns. As in Figure 15, the signal is not correlated with topography and thus is mainly from effects of water vapor in the troposphere.

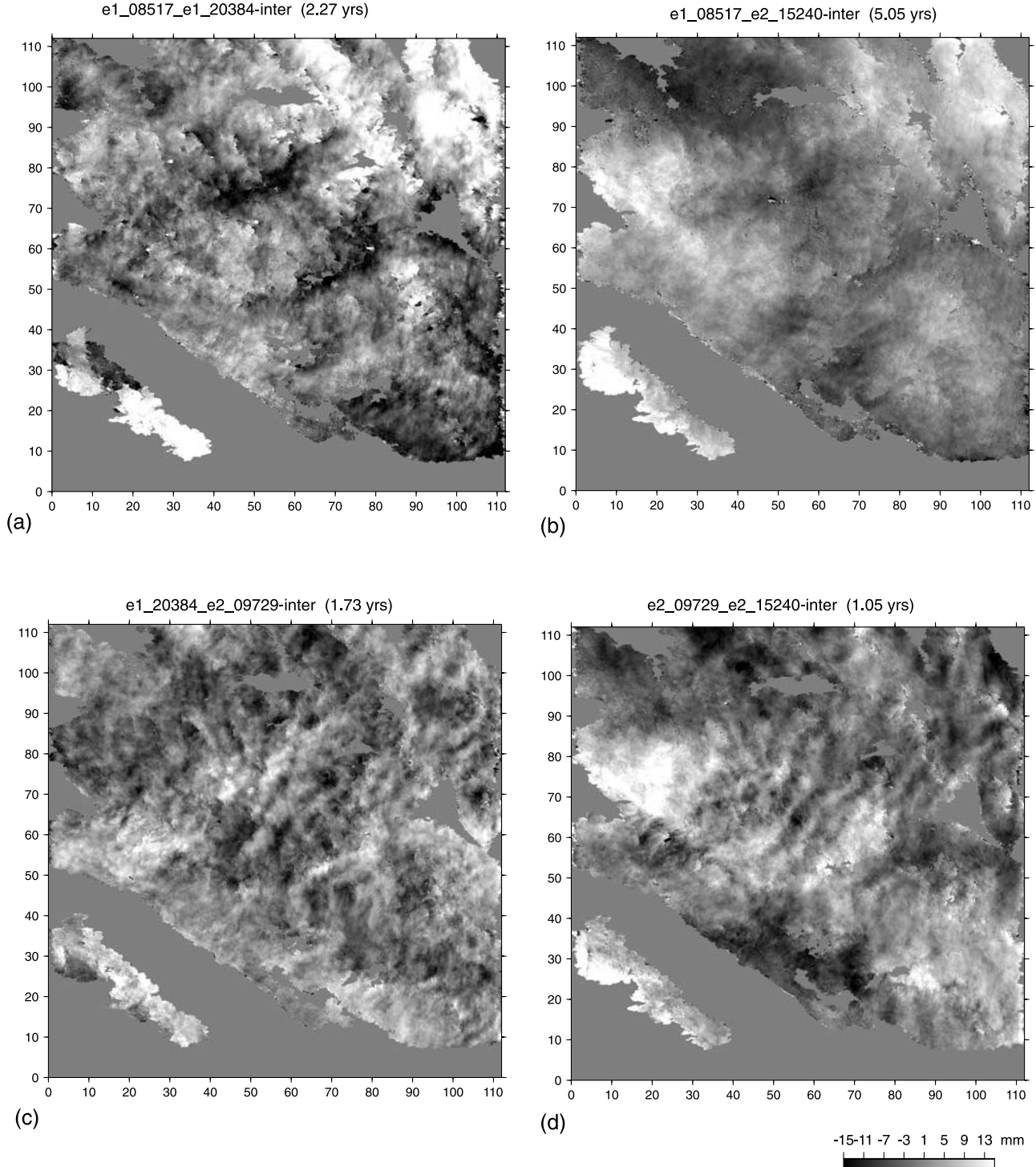
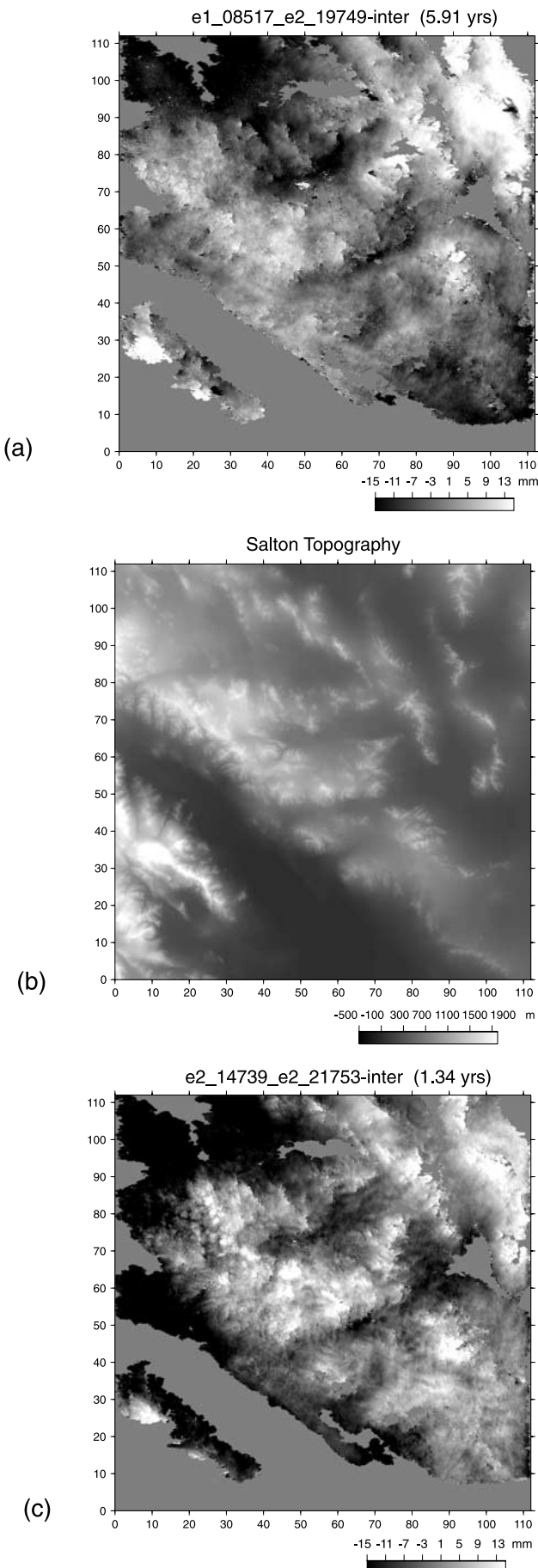


Figure 17. Same as Figure 15, but for (a) $e1_08517_e1_20384$, (b) $e1_08517_e2_15240$, (c) $e1_20384_e2_09729$ and (d) $e2_09729_e2_15240$. Comparison indicates some long-wavelength atmospheric signal in images $e1_08517$ and $e2_15240$ and short-wavelength atmospheric signal in images $e1_20384$ and $e2_09729$.

stack many interferograms over long time spans to minimize tropospheric effects and isolate the deformation signal. This allows us to cover a much broader range of both baselines and time scales and will hopefully provide a more complete characterization of the nature of the tropospheric effects for the region.

[36] First, we show the result of removing both the interseismic deformation signal and a residual plane from three interferograms formed from three SAR acquisitions (Figure 15). Atmospheric residuals range from -15 to 15 mm, and are independent of the time span between images. We selected this interferogram triplet such that two



of the three display common patterns while the third does not so the characteristic atmospheric signal can be isolated to a single SAR acquisition time. In the first example (Figure 15), images (a) and (b) both display atmospheric “ripples” having a characteristic wavelength of 15–20 km, but the signal is not observed in interferogram (c). We conclude that e1_09018 is the source of the gravity waves.

[37] Similarly, the example shown in Figure 16 has shorter-wavelength ripples (2–3 km) in interferograms (a) and (c) but not in (b). We conclude that the ripples come from SAR acquisition e2_11733. In addition to the ripples, interferograms (a) and (b) display wide blotches of the same sign on the western part of the area (labeled A); this atmospheric signal comes from e2_10731. The blotch signals in e2_10731 are probably due to precipitating cumulonimbus clouds [see Hanssen *et al.*, 1999], while the rolls in e2_11733 are likely gravity waves. One can observe other large scale signals that are common to (a) and (c) that are related to a larger scale atmospheric phenomenon (label B).

[38] In most instances, using ERS data, one cannot isolate the atmospheric signal to a particular SAR acquisition either because the signals are chaotic or because not all elements of the triplet can be constructed. Such an example is shown in Figure 17 where atmospheric ripples are apparent (lower panels). We are able to isolate some long-wavelength atmospheric signal in images e1_08517 and e2_15240 and short-wavelength atmospheric signal in images e1_20384 and e2_09729. However, there is no distinct pattern to indicate a definitive cause for the variations in atmospheric signal. Thus, the signal is probably distributed among all of the SAR acquisitions.

[39] The final interferogram examples (Figure 18) display atmospheric signals that are highly correlated with topography and are thus related to vertical stratification in the troposphere at elevations less than the highest peak (~ 2500 m). The center panel (b) in Figure 13 is the topography derived from a USGS grid and a stack of 25 short time span interferograms [Sandwell and Sichoix, 2000]. Note the correlation between the interferograms and topography is more complicated than a simple scale factor, perhaps reflecting spatial variations in the vertical stratification. While a correlation with topography could also be due to topographic error, we rule this out as a possibility because the topographic error is less than 10 m [Sandwell and Sichoix, 2000]. For baselines of 134 and 82 m (Figures 18a and 18c), the topographic phase error is less than 3.8 mm and 2.3 mm, respectively, while the observed phase variations are more than 30 mm. A quantitative correlation between the residual phase and the topography could be used to isolate the effect due to vertical stratification.

Figure 18. (opposite) Atmospheric noise due to topography illustrated in interferograms (a) e1_08517_e2_19749 and (c) e2_14739_e2_21753, compared with Figure 18b the topography (in meters) for the study region. The residuals in Figures 18a and 18c mimic patterns seen in Figure 18b, indicating the main contribution to the atmospheric errors in these interferograms is from vertical stratification of the atmosphere due to topography, rather than from water vapor in the troposphere.

Table 3. Atmospheric Error Statistics for All Interferograms^a

Image	Time Span	Number of Data Used	Mean, mm	σ , mm
Entire Stack (Deformation)	1.00	12822657	-0.40	1.41
e1_04008_e1_22388	3.51	12729530	2.30	10.73
e1_04008_e2_02715	3.52	12640483	1.36	11.08
e1_04008_e2_04218	3.80	12724527	-0.52	15.02
e1_04008_e2_27765	8.31	12476377	1.91	14.02
e1_04509_e1_20885	3.13	12429082	-0.23	13.59
e1_04509_e1_21753	7.44	12580644	1.78	12.11
e1_04509_e2_23757	7.44	12580644	1.78	12.11
e1_04509_e2_25260	7.73	12719124	2.22	14.60
e1_08517_e1_20384	2.27	12652573	1.79	8.05
e1_08517_e1_23390	2.84	12743944	3.95	8.69
e1_08517_e2_09228	3.90	12787240	2.15	8.65
e1_08517_e2_13737	4.76	12772228	2.45	7.12
e1_08517_e2_15240	5.05	12763131	1.66	6.01
e1_08517_e2_15741	5.15	12716073	5.15	12.17
e1_08517_e2_19749	5.91	12558454	0.21	8.20
e1_08517_e2_28266	7.54	12621014	2.09	8.39
e1_09018_e1_23891	2.84	12753806	1.83	7.23
e1_09018_e2_04218	2.85	11593768	2.74	7.80
e1_20384_e1_25394	0.95	12810794	1.26	7.26
e1_20384_e2_09729	1.73	12798180	0.38	5.21
e1_20384_e2_19749	3.64	12794909	-0.48	4.57
e1_20384_e2_24258	4.51	12747593	-2.97	10.56
e1_20885_e2_21753	3.93	12795837	-0.47	9.20
e1_22889_e2_05721	0.48	12812462	0.34	7.52
e1_22889_e2_24258	4.03	12783303	0.17	6.56
e1_23390_e2_13737	1.92	12767254	-0.53	6.67
e1_23390_e2_15741	2.30	12808346	3.22	7.66
e1_23390_e2_26262	4.32	12691101	-0.73	8.70
e1_23891_e2_23256	3.64	12735269	1.34	6.33
e1_23891_e2_27765	4.51	12690805	5.22	10.14
e1_25394_e2_10731	0.96	12814597	-1.40	6.26
e1_25394_e2_24258	3.55	12762393	-3.24	13.34
e2_03216_e2_14739	2.20	12797624	1.44	6.12
e2_03216_e2_21753	3.55	12761718	0.08	5.97
e2_03216_e2_24258	4.02	12756666	2.40	15.20
e2_05721_e2_14238	1.63	12804551	0.90	9.28
e2_05721_e2_24258	3.55	12780326	1.31	14.07
e2_09729_e2_15240	1.05	12804438	-0.12	5.66
e2_09729_e2_28266	3.55	12797232	-1.65	7.26
e2_10230_e2_26262	3.07	12771967	-1.74	9.64
e2_10731_e2_11733	0.19	12821784	0.91	7.75
e2_10731_e2_14238	0.67	12812598	-0.85	7.07
e2_10731_e2_19749	1.73	12795239	-0.39	4.61
e2_11733_e2_14238	0.48	12812037	-1.81	9.69
e2_11733_e2_19749	1.53	12799322	-1.28	8.57
e2_11733_e2_24258	2.40	12795679	-3.53	9.86
e2_13737_e2_15741	0.38	12787232	4.55	11.37
e2_13737_e2_28266	2.78	12781273	-1.18	6.29
e2_14238_e2_19749	1.05	12776497	0.32	6.65
e2_14238_e2_24258	1.92	12810522	-1.25	7.74
e2_14739_e2_21753	1.34	12763047	-1.70	9.19
e2_14739_e2_24258	1.82	12732988	-0.90	7.37
e2_15240_e2_26763	2.21	12745648	5.21	11.63
e2_15741_e2_26763	2.11	12605092	0.58	13.27
e2_19749_e2_24258	0.86	12761928	-2.17	10.27
e2_19749_e2_28266	1.63	12780606	0.12	5.84
e2_21753_e2_23757	0.38	12813805	0.74	8.09
e2_23256_e2_26262	0.58	12795684	-0.31	8.68
e2_23256_e2_27765	0.86	12598397	4.51	12.16
e2_23757_e2_25260	0.29	12808983	-1.89	5.82
Median	2.78	12771967	0.34	8.39
SCEC Phase Model	1.00	21504000	0.26	0.51

^aMean and standard deviation for each interferogram after subtracting the deformation signal (Entire Stack, which has been corrected for orbit error). The standard deviation of the atmospheric signal for most of the interferograms is <15 mm.

[40] Tables 1 and 3 provide the mean and variance for each of our 60 interferograms. The values in Table 3 were derived from interferograms where the secular deformation derived from the entire stack of 60 interferograms was removed. The standard deviation for the images is less than 15 mm for most of the interferograms and the median of all of the standard deviations is 8.39 mm. Table 1 categorizes images into their respective time frames - Interseismic Stack, Hector Stack and Landers Stack - to isolate different types of deformation (triggered slip versus interseismic creep). When shorter stack intervals are used, the standard deviation is typically less than 10 mm.

9. Conclusions

[41] Along the southern San Andreas, InSAR can be used to detect the near field movement of the fault in regions of little vegetation. For areas of partial decorrelation in the interferograms (cropland, populated areas, etc.), the use of permanent scatterers slightly improves the coherence, which increases the area where the phase can be unwrapped. Since the stack of interferograms is the union of the unwrapped phase of the individuals, slight improvements in coherence can lead to significant improvements in the stack. Further improvements in coherence are provided by multilook averaging, but this reduces the spatial resolution of the final LOS displacement maps.

[42] Near the Salton Sea, we found evidence of triggered slip along the entire section of the San Andreas due to the 1992 Landers earthquake, but saw mostly far-field motion from the 1999 Hector Mine earthquake. The amount of interseismic creep varies both temporally and spatially, with the largest values between Desert Beach and Durmid Hill and the smallest values between Durmid Hill and Bombay Beach. At the far southeast end of the fault, there is a large deflating region near the Coachella Canal that appears to be caused by excess groundwater removal along the unlined section of the canal.

[43] **Acknowledgments.** Some of the figures were created using the GMT software of Wessel and Smith [1991]. Duncan Agnew provided a computer program to create a grid interpolating the SCEC velocity model at specific points. Reviews by Roland Bürgmann and Freysteinn Sigmundsson led to a considerable improvement in our slip model and in the organization of this paper. This work was supported by a Department of Defense, National Defense Science and Engineering Graduate Fellowship (S. N. Lyons), NASA Earth Systems Science Fellowship (S. N. Lyons), and NSF Earth Sciences grant NSF EAR-0105896 (D. T. Sandwell).

References

- Bennett, R. A., W. Rodi, and R. E. Reilinger, Global Positioning System constraints on fault slip rates in southern California and northern Baja, Mexico, *J. Geophys. Res.*, 101, 21,943–21,960, 1996.
- Bilham, R., and P. Williams, Sawtooth segmentation and deformation processes on the southern San Andreas Fault, California, *Geophys. Res. Lett.*, 12, 557–560, 1985.
- Bodin, P., R. Bilham, J. Behr, J. Gomberg, and K. W. Hudnut, Slip triggered on southern California faults by the 1992 Joshua Tree, Landers and Big Bear earthquakes, *Bull. Seismol. Soc. Am.*, 84, 806–816, 1994.
- Bürgmann, R., D. Schmidt, R. M. Nadeau, M. d'Alessio, E. Fielding, D. Manaker, T. V. McEvilly, and M. H. Murray, Earthquake potential along the northern Hayward fault, California, *Science*, 289, 1178–1182, 2000.
- Byerlee, J. D., Friction of rocks, *Pure Appl. Geophys.*, 116, 615–626, 1978.
- Chunchuzov, I., P. W. Vachon, and X. Li, Analysis and modelling of atmospheric gravity waves observed in RADARSAT SAR images, *Remote Sens. Environ.*, 74, 343–361, 2000.

- Ferretti, A., C. Prati, and F. Rocca, Nonlinear subsidence rate estimation using permanent scatterers in differential SAR interferometry, *IEEE Trans. Geosci. Remote Sens.*, **38**, 2202–2212, 2000.
- Ferretti, A., C. Prati, and F. Rocca, Permanent scatterers in SAR interferometry, *IEEE Trans. Geos. Remote Sens.*, **39**, 8–20, 2001.
- Hanssen, R. F., Radar interferometry: Data interpretation and error analysis, Ph.D. thesis, Tech. Univ., Delft, 2001.
- Hanssen, R. F., T. M. Weckwerth, H. A. Zebker, and R. Klees, High-resolution water vapor mapping from interferometric radar measurements, *Science*, **283**, 1297–1299, 1999.
- Harris, R. A., and P. Segall, Detection of a locked zone at depth on the Parkfield, California, segment of the San Andreas fault, *J. Geophys. Res.*, **92**, 7945–7962, 1987.
- Hauksson, E., and L. M. Jones, Interseismic background seismicity of the southern San Andreas Fault, California, paper presented at the 3rd Conference on Tectonic Problems of the San Andreas Fault System, Stanford Univ., Stanford, Calif., 6–8 Sept. 2000.
- Haynes, M., New developments in wide-area precision surveying from space, *Mapp. Aware.*, **13**, 40–43, 1999.
- King, G. C. P., R. S. Stein, and J. Lin, Static stress changes and the triggering of earthquakes, *Bull. Seismol. Soc. Am.*, **84**, 935–953, 1994.
- Langbein, J., A. McGarr, M. J. S. Johnston, and P. W. Harsh, Geodetic measurements of postseismic crustal deformation following the 1979 Imperial Valley earthquake, California, *Bull. Seismol. Soc. Am.*, **73**, 1203–1224, 1983.
- Lisowski, M., and W. H. Prescott, Short-range distance measurements along the San Andreas fault system in central California, 1975 to 1979, *Bull. Seismol. Soc. Am.*, **71**, 1607–1624, 1981.
- Lorenzetti, E., and T. E. Tullis, Geodetic predictions of a strike-slip fault model: Implications for intermediate- and short-term earthquake prediction, *J. Geophys. Res.*, **94**, 12,343–12,361, 1989.
- Louie, J. N., C. R. Allen, D. C. Johnson, P. C. Haase, and S. N. Cohn, Fault slip in Southern California, *Bull. Seismol. Soc. Am.*, **75**, 811–833, 1985.
- Massonnet, D., and K. L. Feigl, Radar interferometry and its applications to changes in the Earth's surface, *Rev. Geophys.*, **36**, 441–500, 1998.
- Mattar, K. E., A. L. Gray, D. Gedtner, and P. W. Vachon, Interferometry for mapping and terrain displacement: Effect of anisotropic propagation, in *Geomatics in the Era of RADARSAT (GER'97)* [CD-ROM], Ottawa, Canada, 1997.
- Richards-Dinger, K. B., and P. M. Shearer, Earthquake locations in southern California obtained using source specific station terms, *J. Geophys. Res.*, **105**, 10,939–10,960, 2000.
- Rosen, P. A., S. Hensley, I. R. Joughin, F. K. Li, S. N. Madsen, E. Rodriguez, and R. M. Goldstein, Synthetic Aperture Radar Interferometry, *Proc. IEEE*, **88**, 333–382, 2000.
- Rymer, M., Triggered surface slips in the Coachella Valley area associated with the 1992 Joshua Tree and Landers, California, earthquakes, *Bull. Seismol. Soc. Am.*, **90**, 832–848, 2000.
- Rymer, M., J. Boatwright, L. C. Seekins, J. D. Yule, and J. Liu, Triggered surface slips in the Salton Trough associated with the 1999 Hector Mine earthquakes, *Bull. Seismol. Soc. Am.*, **92**, 1300–1317, 2002.
- Sandwell, D., and D. Agnew, Strain accumulation and fault creep on the southern San Andreas Fault: 1992 to present, *Eos Trans. AGU*, **80**(46), Fall Meet. Suppl., F692, 1999.
- Sandwell, D., and L. Sichoux, Topographic recovery from stacked ERS interferometry and a low resolution digital elevation model, *J. Geophys. Res.*, **105**, 28,211–28,222, 2000.
- Sandwell, D. T., and E. J. Price, Phase gradient approach to stacking interferograms, *J. Geophys. Res.*, **103**, 30,183–30,204, 1998.
- Savage, J. C., Equivalent strike-slip earthquake cycles in half-space and lithosphere-asthenosphere earth models, *J. Geophys. Res.*, **95**, 4873–4879, 1990.
- Savage, J. C., and R. O. Burford, Discussion of paper by C. H. Scholz and T. J. Fitch, Strain accumulation along the San Andreas Fault, *J. Geophys. Res.*, **76**, 6469–6479, 1971.
- Savage, J. C., and M. Lisowski, Inferred depth of creep on the Hayward Fault, central California, *J. Geophys. Res.*, **98**, 787–793, 1993.
- Sieh, K. E., Slip rate across the San Andreas Fault and prehistoric earthquakes at Indio, California, *Eos Trans. AGU*, **67**, 1200, 1986.
- Stein, R. S., G. C. P. King, and J. Lin, Change in failure stress on the southern San Andreas fault system caused by the 1992 Magnitude = 7.4 Landers earthquake, *Science*, **258**, 1328–1332, 1992.
- Sylvester, A. G., R. Bilham, M. Jackson, and S. Barrientos, Aseismic growth of Durmid Hill, southeasternmost San Andreas Fault, California, *J. Geophys. Res.*, **98**, 14,233–14,243, 1993.
- Thatcher, W., Nonlinear strain buildup and the earthquake cycle on the San Andreas Fault, *J. Geophys. Res.*, **88**, 5893–5902, 1983.
- Tse, S. T., and J. R. Rice, Crustal earthquake instability in relation to depth variation of frictional slip parameters, *J. Geophys. Res.*, **91**, 9452–9572, 1986.
- Vachon, P. W., J. A. Johannessen, and D. B. Browne, ERS-1 SAR images of atmospheric gravity waves, *IEEE Trans. Geosci. Remote Sens.*, **33**, 1014–1025, 1995.
- Vachon, P. W., O. M. Johannessen, and J. A. Johannessen, An ERS-1 synthetic aperture radar image of atmospheric lee waves, *J. Geophys. Res.*, **99**, 22,483–22,490, 1994.
- Vincent, P., J. B. Rundle, R. Bilham, and S. M. Buckley, Aseismic creep along the San Andreas and Superstition Hills faults with uplift at Durmid Hill, southernmost San Andreas fault, CA measured by radar interferometry, *Eos Trans. AGU*, **79**(45), Fall Meet. Suppl., F45, 1998.
- Wdowinski, S., Y. Sudman, and Y. Bock, Distribution of interseismic deformation along the San Andreas fault system, southern California, *Geophys. Res. Lett.*, **28**, 2321–2324, 2001.
- Weertman, J., Continuous distribution of dislocations on faults with finite friction, *Bull. Seismol. Soc. Am.*, **54**, 1035–1058, 1964.
- Wessel, P., and W. H. F. Smith, Free software helps map and display data, *Eos Trans. AGU*, **72**, 441, 445–446, 1991.
- Working Group on California Earthquake Probabilities, Seismic hazard in southern California: Probable earthquakes, 1994 to 2024, *Bull. Seismol. Soc. Am.*, **85**, 379–439, 1995.
- Zebker, H. A., P. A. Rosen, and S. Hensley, Atmospheric effects in interferometric synthetic aperture radar surface deformation and topographic maps, *J. Geophys. Res.*, **102**, 7547–7563, 1997.

S. Lyons and D. Sandwell, Scripps Institution of Oceanography, La Jolla, CA 92093-0225, USA. (slyons@radar.ucsd.edu)